Intrinsic spin Hall effect and orbital Hall effect in 4*d* and 5*d* transition metals

T. Tanaka,[1] H. Kontani,[1] M. Naito,[1] T. Naito,[1] D. S. Hirashima,[1] K. Yamada,[2] and J. Inoue[3]
[1]*Department of Physics, Nagoya University, Furo-cho, Nagoya 464-8602, Japan*
[2]*Engineering, Ritsumeikan University, 1-1-1 Noji Higashi, Kusastu, Shiga 525-8577, Japan*
[3]*Department of Applied Physics, Nagoya University, Furo-cho, Nagoya 464-8602, Japan*
(Received 8 November 2007; revised manuscript received 26 February 2008; published 11 April 2008)

We study the intrinsic spin Hall conductivity (SHC) in various 5*d* transition metals (Ta, W, Re, Os, Ir, Pt, and Au) and 4*d* transition metals (Nb, Mo, Tc, Ru, Rh, Pd, and Ag) based on the Naval Research Laboratory tight-binding model, which enables us to perform quantitatively reliable analysis. In each metal, the obtained intrinsic SHC is independent of resistivity in the low resistive regime ($\rho < 50\ \mu\Omega\,\mathrm{cm}$) whereas it decreases in proportion to ρ^{-2} in the high resistive regime. In the low resistive regime, the SHC takes a large positive value in Pt and Pd, both of which have approximately nine *d* electrons per ion ($n_d=9$). On the other hand, the SHC takes a large negative value in Ta, Nb, W, and Mo, where $n_d<5$. In transition metals, a conduction electron acquires the trajectory-dependent phase factor that originates from the atomic wave function. This phase factor, which is reminiscent of the Aharonov–Bohm phase, is the origin of the SHC in paramagnetic metals and that of the anomalous Hall conductivity in ferromagnetic metals. Furthermore, each transition metal shows huge and positive *d*-orbital Hall conductivity (OHC), independent of the strength of the spin-orbit interaction. Since the OHC is much larger than the SHC, it will be possible to realize an *orbitronics device* made of transition metals.

DOI: 10.1103/PhysRevB.77.165117 PACS number(s): 72.25.Ba, 72.25.−b, 75.47.−m

I. INTRODUCTION

In recent years, spin Hall effect (SHE) in transition metals has received considerable attention due to its fundamental as well as technological interest. The SHE is the phenomenon that an electric field induces a spin current in a transverse direction. Recent experimental efforts have revealed that many metallic compounds show sizable spin Hall conductivity (SHC).[1–4] In particular, Pt shows a huge SHC at room temperature.[1,4] The observed SHC in Pt is $\sim 240\hbar e^{-1}\ \Omega^{-1}\,\mathrm{cm}^{-1}$[4], which is about 10^4 times larger than the SHC reported in *n*-type semiconductors. This unexpected experimental fact cannot be understood based on the simple electron gas models for semiconductors.[5,6] To elucidate the origin of the huge SHE in transition metals, several authors have studied the SHC based on the multiorbital tight-binding models[7,8] and the first-principles band calculation.[9] Reference 7 showed that the orbital degrees of freedom in transition ions, which are absent in electron gas models, are crucial to realize the huge SHE in various transition metals.

The SHE has a close relationship to the anomalous Hall effect (AHE) in the presence of the magnetization **M**, where charge current is induced by an electric field **E** parallel to $\mathbf{M}\times\mathbf{E}$. In 1954, Karplus and Luttinger[10] (KL) solved the kinetic equation for ↑-, ↓-spin electrons in the multiband system with the *z* component of the atomic spin-orbit interaction (SOI) $\lambda_1\Sigma_l(\hat{l}_z\hat{s}_z)_l$. Under the electric field $\mathbf{E}\|\hat{y}$, they showed that the ↑-spin and ↓-spin electrons move to the opposite direction parallel to the $\hat{x}$ axis. Their analysis strongly suggests that the AHE (SHE) occurs in ferromagnetic (paramagnetic) multiband systems with the SOI. The Hall effect studied by KL, which is due to the interband particle-hole excitation and is independent of impurity scattering, is called the "intrinsic Hall effect." However, this explanation, according to the KL theory, is too naive in that they omitted the *x* and *y* components of the SOI $\lambda_2\Sigma_l(\hat{l}_x\hat{s}_x+\hat{l}_y\hat{s}_y)_l$. In the case of $\lambda_2\neq 0$, there is no simple relation between SHE and AHE since $s_z=\pm 1/2$ is not a good quantum number.

Note that KL did not make mention of the SHC. The analogous relationship between AHE and SHE was first pointed out by Dyakonov and Perel.[11]

After KL, theories of the intrinsic AHE[12–23] and SHE[5–8,24–26] have been improved based on several specific theoretical models. Kontani and Yamada[15] studied the intrinsic AHE based on the periodic Anderson model by considering the SOI unperturbatively. By using the microscopic Fermi liquid theory, they derived the general expression for the anomalous Hall conductivity (AHC) by considering all the self-energy correction and the current vertex correction (CVC). Their study clarified that the intrinsic AHE (due to the KL mechanism) remains finite even if all of the scattering processes are taken into account rigorously, in contrast to Smit's claim.[27] The obtained general expression succeeded in explaining the huge AHC observed in heavy-fermion systems. It was found that the large anomalous velocity, which is not perpendicular to the Fermi surface and is the origin of the AHE, is caused by the $\boldsymbol{k}$ derivative of the phase factor in the *c*-*f* mixing potential. That is, the *f*-orbital degree of freedom is significant for the AHE. Later, AHE in *d*-electron systems has been studied intensively.[17,20–22]

Recently, Murakami *et al.*[5] and Sinova *et al.*[6] calculated the intrinsic SHC in the Luttinger model and the two-dimensional Rashba model, respectively. Later, several authors studied the disorder effect on SHC.[24,28,29] Inoue *et al.*[23] proved that the intrinsic SHE in the Rashba model vanishes due to the cancellation by the CVC due to impurities. In analogy to the quantum charge Hall effect, it has been predicted that a large (and quantized) SHC may be realized in massless Dirac electron systems, when the chemical potential lies inside the gap induced by the SOI. This mechanism

 ©2008 The American Physical Society

has been predicted to be realized in some semiconductors[30] and in graphene.[31]

However, in usual metallic systems, the existence of the Dirac point just at the Fermi level cannot be expected in general. Therefore, other novel mechanisms for large SHC are expected to be realized in Pt and other transition metals. In fact, Kontani *et al.*[7] presented the first report on the theoretical study of SHE in transition metal compound Sr_2RuO_4, which has no Dirac-cone-type dispersion at the Fermi level. They found that the origin of the huge Hall effect is the "effective Aharonov–Bohm (AB) phase" induced by *d*-orbital degrees of freedom, which are absent in semiconductors and in graphene. This mechanism is expected to produce huge SHE in various multiorbital *d*-electron systems universally. Later, Refs. 8 and 9 succeeded in reproducing the SHC in Pt theoretically.

In the present paper, we study the intrinsic SHE in various 4*d* and 5*d* transition metals by taking account of their realistic band structures. We employ the Naval Research Laboratory tight-binding (NRL-TB) model,[32,33] which enables us to construct nine-orbital $(s+p+d)$ tight-binding models for each transition metal. We find that both Pt $(5d^9)$ and Pd $(4d^9)$, which have a face-centered cubic (fcc) structure, show large positive SHCs. On the other hand, the SHCs take large negative values in Ta $(5d^4)$, Nb $(4d^4)$, W $(5d^5)$, and Mo $(4d^5)$, which have body-centered cubic (bcc) structures. We find that the SHC changes smoothly with the electron number $n=n_s+n_d$ regardless of the changes of the crystal structure, where n_α represents the number of electrons on the α orbital. Among them, Pt shows the largest SHC in the low resistive regime. Usually, intrinsic SHC is independent of resistivity in the low resistive regime $(\rho \lesssim 50\ \mu\Omega\ \mathrm{cm})$, whereas it decreases in proportion to ρ^{-2} in the high resistive regime. However, we find a condition that the intrinsic SHC decreases as ρ approaches zero in the low resistive regime. This anomalous phenomenon may be realized in Ta.

Furthermore, we study the *d*-orbital Hall effect (OHE), which is the phenomenon that an electric field induces a *d*-orbital current in a transverse direction.[7,8] We find that the *d*-orbital Hall conductivity (OHC) is almost 1 order of magnitude larger than the SHC, since the OHC occurs even in the absence of the SOI. By using the large OHE in transition metals, we will be able to construct an *orbitronics device* made of transition metals. In a later publication, we will present an intuitive (semiclassical) explanation for the origin of the OHC.[34]

Finally, we comment on the extrinsic Hall effect. In 1958, Smit[35] studied the AHE due to the asymmetric scattering around the impurity in the presence of spin-orbit coupling, which is called the skew-scattering mechanism. The AHC due to skew scattering is proportional to ρ^{-1} if elastic scattering is dominant. In 1970, Berger proposed another mechanism of extrinsic Hall effect: the side jump due to impurities.[36] This mechanism gives the AHC in proportion to ρ^{-2}. Both extrinsic Hall effects vanish where the inelastic scattering due to electron-electron or electron-phonon interaction is dominant over the elastic scattering. Both mechanisms (the skew scattering and the side jump) cause the extrinsic SHE.[37–40] In the present paper, we do not study the extrinsic SHE, which is sensitive to the character of the impurity potential. It is an important future problem to study the extrinsic SHE in realistic multiorbital tight-binding models.

TABLE I. The crystal structure, electron number per atom, and the coupling constant λ of SOI for various transition metals. $(m_d d^{n_d} m_s s^{n_s})$ represent the electronic configuration of an isolated atom. Here, m_d and m_s are the main quantum numbers, and n_s and n_d are the numbers of electrons on *s* and *d* orbitals, respectively, bcc, hcp, and fcc represent a body-centered cubic, hexagonal closed packed, and face-centered cubic, respectively.

Metals	Structure	Electron number	SOI (Ry)
Nb	bcc	5 $(4d^4 5s^1)$	0.006
Mo	bcc	6 $(4d^5 5s^1)$	0.007
Tc	hcp	7 $(4d^6 5s^1)$	0.009
Ru	hcp	8 $(4d^7 5s^1)$	0.01
Rh	fcc	9 $(4d^8 5s^1)$	0.011
Pd	fcc	10 $(4d^{10} 5s^0)$	0.013
Ag	fcc	11 $(4d^{10} 5s^1)$	0.019
Ta	bcc	5 $(5d^3 6s^2)$	0.023
W	bcc	6 $(5d^4 6s^2)$	0.027
Re	hcp	7 $(5d^5 6s^2)$	0.025
Os	hcp	8 $(5d^6 6s^2)$	0.025
Ir	fcc	9 $(5d^9 6s^0)$	0.025
Pt	fcc	10 $(5d^9 6s^1)$	0.03
Au	fcc	11 $(5d^{10} 6s^1)$	0.03

II. MODEL AND HAMILTONIAN

In the present study, we use the NRL-TB model[32,33] to obtain the band structure in various transition metals. Here, we shortly explain this model. The NRL-TB model employs the scheme of two-center and nonorthogonal Slater–Koster (SK) Hamiltonian.[41] The SK parameters are represented with distance- and environment-dependent parameters that are determined so that the total energy and the band structures agree with those obtained by full-potential linear augmented plane wave local density approximation calculations. The root mean square error in the fitting is about 0.002–0.004 Ry.[42] This fitting error is small enough to perform reliable numerical calculations. To describe the electronic state in 4*d* (5*d*) metals, we consider 5*s*, 5*p*, and 4*d* (6*s*, 6*p*, and 5*d*) orbitals, that is, we consider nine orbitals per atom. Hopping integrals between a pair of atoms are then expressed with ten SK parameters ($ss\sigma$, $sp\sigma$, $pp\sigma$, $pp\pi$, $sd\sigma$, $pd\sigma$, $pd\pi$, $dd\sigma$, $dd\pi$, and $dd\delta$). In this study, we consider hopping (and overlap) integrals up to sixth nearest neighbor sites for metals with fcc and bcc structures, and up to ninth nearest neighbor sites for hexagonal closed packed (hcp) structures.

Table I shows the crystal structure, electron number per atom, and the coupling constant λ of SOI $\lambda\Sigma_i \hat{l}_i \hat{s}_i$ $(i=x,y,z)$ for various 4*d* and 5*d* transition metals. $(m_d d^{n_d} m_s s^{n_s})$ represent the electronic configuration of an isolated atom, where

m_d and m_s are the main quantum number, and n_s and n_d are the number of electrons on s and d orbitals, respectively. In this table, we set $\lambda=0.03$ Ry for a $5d$ electron in Pt and $\lambda=0.013$ Ry for a $4d$ electron in Pd, according to optical spectroscopy.[43] For other $4d$ and $5d$ transition metals, we used Herman–Skillman atomic spin-orbit parameters:[44] These parameters had been calculated by using the self-consistent Hartree–Fock–Slater atomic functions. Here, we consider only the d-orbital SOI and neglect other SOI terms that may possess a $\boldsymbol{k}$ dependence. Hereafter, we set the unit of energy Ry as 1 Ry=13.6 eV.

In the presence of SOI for $4d$ or $5d$ electrons, the total Hamiltonian is given by

$$\hat{H} = \begin{pmatrix} \hat{H}_0 + \lambda \hat{l}_z/2 & \lambda(\hat{l}_x - i\hat{l}_y)/2 \\ \lambda(\hat{l}_x + i\hat{l}_y)/2 & \hat{H}_0 - \lambda \hat{l}_z/2 \end{pmatrix}, \tag{1}$$

where the first and second rows (columns) correspond to $s_z=+\hbar/2$ ($\uparrow$ spin) and $s_z=-\hbar/2$ ($\downarrow$ spin). $\hat{H}_0$ is a 9×9 matrix given by the NRL-TB model for bcc and fcc structures. In the case of a hcp structure, $\hat{H}_0$ is an 18×18 matrix, since a unit cell contains two atoms. The matrix elements of $\boldsymbol{l}$ for the d orbital are given by[43]

$$l_x = \begin{pmatrix} 0 & 0 & -i & 0 & 0 \\ 0 & 0 & 0 & -i & -i\sqrt{3} \\ i & 0 & 0 & 0 & 0 \\ 0 & i & 0 & 0 & 0 \\ 0 & i\sqrt{3} & 0 & 0 & 0 \end{pmatrix}, \tag{2}$$

$$l_y = \begin{pmatrix} 0 & i & 0 & 0 & 0 \\ -i & 0 & 0 & 0 & 0 \\ 0 & 0 & 0 & -i & i\sqrt{3} \\ 0 & 0 & i & 0 & 0 \\ 0 & 0 & -i\sqrt{3} & 0 & 0 \end{pmatrix}, \tag{3}$$

$$l_z = \begin{pmatrix} 0 & 0 & 0 & 2i & 0 \\ 0 & 0 & i & 0 & 0 \\ 0 & -i & 0 & 0 & 0 \\ -2i & 0 & 0 & 0 & 0 \\ 0 & 0 & 0 & 0 & 0 \end{pmatrix}, \tag{4}$$

where the first to fifth rows (columns) correspond to d orbitals xy, yz, zx, x^2-y^2, and $3z^2-r^2$, respectively.

In the NRL-TB model, we use the nonorthogonal basis since the atomic wave functions of different sites are not orthogonal:

$$\int d\boldsymbol{r}\,\phi_\alpha^*(\boldsymbol{r}-\boldsymbol{R}_i)\phi_\beta(\boldsymbol{r}-\boldsymbol{R}_{i'}) = O_{\alpha\beta}(\boldsymbol{R}_i-\boldsymbol{R}_{i'}), \tag{5}$$

where $\phi_\alpha(\boldsymbol{r}-\boldsymbol{R}_i)$ represents the atomic wave function at the ith site, α and β are orbital state indices, and $O_{\alpha\beta}(\boldsymbol{R}_i-\boldsymbol{R}_{i'})$ represents the overlap integral between different sites. When the overlap integrals between different sites are negligible, Eq. (5) is simplified as

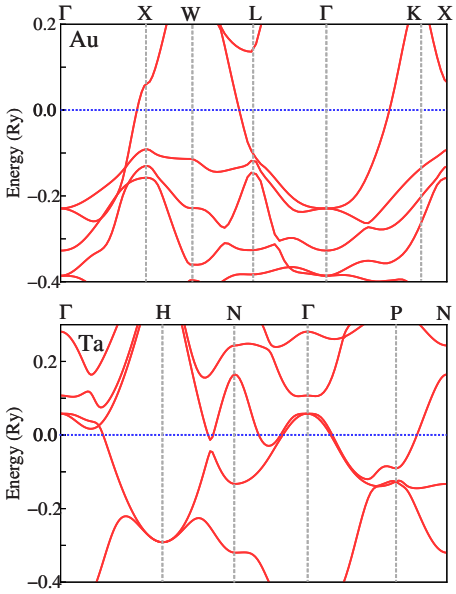

FIG. 1. (Color online) (Upper panel) Band structure of Au. Here, $\Gamma=(0,0,0)$, $X=(\pi,0,0)$, $W=(\pi,\pi/2,0)$, $L=(\pi/2,\pi/2,\pi/2)$, and $K=(3\pi/4,3\pi/4,0)$. (Lower panel) Band structure of Ta. Here, $\Gamma=(0,0,0)$, $H=(\pi,0,0)$, $N=(\pi/2,\pi/2,0)$, and $P=(\pi/2,\pi/2,\pi/2)$. Near the Fermi level, we see that the band structures obtained in the present model agree well with the result of the relativistic first-principles calculation in Refs. 45 and 46

$$O_{\alpha\beta}(\boldsymbol{R}_i-\boldsymbol{R}_{i'}) = \delta_{\alpha\beta}\delta_{ii'}. \tag{6}$$

This approximation is rather appropriate when α and β correspond to d orbitals, since d-orbital atomic wave functions are localized well. However, when α and β are either s or p orbital, $O_{\alpha\beta}(\boldsymbol{R}_i-\boldsymbol{R}_{i'})$ is large even when $i\neq i'$ and, therefore, Eq. (6) is not satisfied.

The band structures obtained for the present model in Au and Ta are shown in Fig. 1. These band structures are derived by taking the overlap integrals between different sites into account correctly. The methods on how to calculate these band structures are explained in Sec. III C. Near the Fermi level, the obtained band structures are in good agreement with the results of the relativistic first-principles calculations.[45,46] Since the Fermi surface is mainly composed of d electrons in the transition metals, in which we study the SHE and OHE, the band structure near the Fermi level is described well when $O_{\alpha\beta}(\boldsymbol{R}_i-\boldsymbol{R}_{i'})$ is approximated by Eq. (6). Therefore, the calculations of SHE and OHE using Eq. (6) seem to give semiquantitatively reliable results.[8] However, for a more quantitative study of SHE and OHE, we need to consider the overlap integrals between different sites.

Until Sec. III C, we will use the simplified overlap integrals given by Eq. (6) to simplify the explanation. In Sec. III C, we will study the SHE and OHE by considering the overlap integrals in Eq. (5) correctly. The 18×18 matrix form of the Green function without impurities is given by $\hat{G}^0(\boldsymbol{k},\omega)=(\omega+\mu-\hat{H})^{-1}$, where μ represents the chemical potential. There is a $\boldsymbol{k}$-dependent unitary matrix $\hat{U}$ that diagonalizes the Hamiltonian $\hat{H}$ as follows:

$$\sum_{\alpha\beta} U^{\dagger}_{l\alpha} H^{\alpha\beta} U_{\beta m} = E^{l}_{\boldsymbol{k}} \delta_{lm}, \tag{7}$$

where α and β are the orbital indices, and l and m are the band indices.

Here, we consider the quasiparticle damping rate $\hat{\Gamma}$, which is given by $[\hat{\Sigma}_{\boldsymbol{k}}(-i0) - \hat{\Sigma}_{\boldsymbol{k}}(+i0)]/2i$, where $\hat{\Sigma}_{\boldsymbol{k}}(\omega)$ is the self-energy matrix. In the Born approximation for $I \ll W_{band}$, $\hat{\Gamma}$ is given by $\hat{\Gamma} = n_{imp} I^2 \frac{1}{2i}[\hat{g}(-i0) - \hat{g}(+i0)]$, where n_{imp} is the impurity concentration, I is the impurity potential, W_{band} is the bandwidth, and $\hat{g}(\omega)$ is the local Green function $\hat{g}(\omega) = \frac{1}{N}\Sigma_{\boldsymbol{k}} \hat{G}(\boldsymbol{k}, \omega)$, respectively. Here, N is the total number of lattice points. In the T-matrix approximation for the general strength of I, $\hat{\Gamma}$ is given by $\hat{\Gamma} = n_{imp} I (1/2i)(\{1/[1 - I\hat{g}(-i0)]\} - \{1/[1 - I\hat{g}(+i0)]\})$. The retarded and advanced Green functions are given by

$$\hat{G}^{R}(\boldsymbol{k}, \omega) = (\omega + \mu - \hat{H} + i\hat{\Gamma})^{-1}, \tag{8}$$

$$\hat{G}^{A}(\boldsymbol{k}, \omega) = (\omega + \mu - \hat{H} - i\hat{\Gamma})^{-1}. \tag{9}$$

In the present model, the charge current operator for the μ direction ($\mu = x, y$) is given by

$$\hat{J}^{C}_{\mu} = \begin{pmatrix} \hat{j}^{C}_{\mu} & 0 \\ 0 & \hat{j}^{C}_{\mu} \end{pmatrix}, \tag{10}$$

where $\hat{j}^{C}_{\mu} = -e\frac{\partial \hat{H}_0}{\partial k_\mu}$, and $-e (e > 0)$ is the electron charge. Here, atomic SOI is not involved in the charge current operator since it is $\boldsymbol{k}$ independent. Also, the s_z-spin current operator $\hat{J}^{S}_{\mu} = \{\hat{J}^{C}_{\mu}, \hat{s}_z\}/2 = (\hat{J}^{C}_{\mu}\hat{s}^{z} + \hat{s}^{z}\hat{J}^{C}_{\mu})/2$ (Refs. 24 and 47) is given by

$$\hat{J}^{S}_{\mu} = (-\hbar/e) \begin{pmatrix} \hat{j}^{C}_{\mu} & 0 \\ 0 & -\hat{j}^{C}_{\mu} \end{pmatrix}, \tag{11}$$

and l_z-orbital current operator is given by

$$\hat{J}^{O}_{x} = \{\hat{j}^{C}_{x}, \hat{l}_z\}/2. \tag{12}$$

We will discuss the validity of these current operators in more detail in Appendix B.

III. SPIN AND ORBITAL HALL CONDUCTIVITIES

A. Spin Hall conductivity and orbital Hall conductivity without overlap integrals between different sites

In this section, we derive the general expressions for the intrinsic SHE and OHE based on the linear-response theory. As we will discuss in Sec. III B, we can safely neglect the CVC in calculating SHC and OHC in the present model. Therefore, the SHC at $T=0$ is given by $\sigma^{z}_{xy} = \sigma^{zI}_{xy} + \sigma^{zII}_{xy}$ according to Streda,[48] where

$$\sigma^{zI}_{xy} = \frac{1}{2\pi N}\sum_{\boldsymbol{k}} \mathrm{Tr}[\hat{J}^{S}_{x}\hat{G}^{R}\hat{J}^{C}_{y}\hat{G}^{A}]_{\omega=0}, \tag{13}$$

$$\sigma^{zII}_{xy} = \frac{-1}{4\pi N}\sum_{\boldsymbol{k}} \int_{-\infty}^{0} d\omega\, \mathrm{Tr}\left[\hat{J}^{S}_{x}\frac{\partial \hat{G}^{R}}{\partial \omega}\hat{J}^{C}_{y}\hat{G}^{R} - \hat{J}^{S}_{x}\hat{G}^{R}\hat{J}^{C}_{y}\frac{\partial \hat{G}^{R}}{\partial \omega} - \langle R \leftrightarrow A \rangle \right]. \tag{14}$$

Here, I and II represent the "Fermi surface term" and the "Fermi sea term," respectively. In the same way, the OHC of the Fermi surface term O^{zI}_{xy} and that of the Fermi sea term O^{zII}_{xy} are respectively given by Eqs. (13) and (14) by replacing $\hat{J}^{S}_{x}$ with the l_z-orbital current operator $\hat{J}^{O}_{x}$ in Eq. (12).

In the Born approximation, the quasiparticle damping rate depends on orbital indices. If $\lambda = 0$, $\hat{\Gamma}$ is diagonal with respect to the orbital: $\hat{\Gamma}_{\alpha\beta} = \gamma_\alpha \delta_{\alpha\beta}$, where α and β are orbital indices. Then, the off-diagonal terms are negligible when $\lambda \ll W_{band}$. γ_α is the quasiparticle damping rate for the α orbital and is proportional to the local density of states (LDOS) for the α orbital, $\rho_\alpha(0)$. In the present model, d-orbital LDOSs are almost equal in magnitude. Therefore, γ_α is approximately independent of α and can be approximated by a constant γ: $\Gamma_{\alpha\beta} = \gamma\delta_{\alpha\beta}$. By using this constant γ approximation, we derive the general expressions for the Fermi surface and Fermi sea terms. In this case, the retarded and advanced Green functions can be diagonalized by using the unitary matrix $\hat{U}$ given by Eq. (7) as follows:

$$\sum_{\alpha\beta} U^{\dagger}_{l\alpha} G^{R}_{\alpha\beta} U_{\beta m} = \frac{\delta_{lm}}{\omega - E^{l}_{\boldsymbol{k}} + i\gamma}, \tag{15}$$

where l and m are the band indices. Therefore, we can rewrite Eqs. (13) and (14) by using $\hat{U}$ as follows:

$$\sigma^{zI}_{xy} = \frac{1}{2\pi N}\sum_{\boldsymbol{k}, l\neq m} (J^{S}_{x})^{ml}(J^{C}_{y})^{lm}\frac{1}{(E^{l}_{\boldsymbol{k}} - i\gamma)(E^{m}_{\boldsymbol{k}} + i\gamma)} = \frac{-1}{2\pi N}\sum_{\boldsymbol{k}, l\neq m} \mathrm{Im}\{(J^{S}_{x})^{ml}(J^{C}_{y})^{lm}\}\mathrm{Im}\left[\frac{1}{(E^{l}_{\boldsymbol{k}} - i\gamma)(E^{m}_{\boldsymbol{k}} + i\gamma)}\right], \tag{16}$$

$$\sigma^{zII}_{xy} = -\frac{1}{2\pi N}\sum_{\boldsymbol{k}, l\neq m} \int_{-\infty}^{0} d\omega\, \mathrm{Im}\{(J^{S}_{x})^{ml}(J^{C}_{y})^{lm}\} \times \mathrm{Im}\left[\frac{1}{(\omega - E^{l}_{\boldsymbol{k}} + i\gamma)^2}\frac{1}{(\omega - E^{m}_{\boldsymbol{k}} + i\gamma)} - \frac{1}{(\omega - E^{l}_{\boldsymbol{k}} + i\gamma)}\frac{1}{(\omega - E^{m}_{\boldsymbol{k}} + i\gamma)^2}\right], \tag{17}$$

where $(J^{S}_{x})^{ml}$ is given by $\Sigma_{\alpha\beta} U^{\dagger}_{m\alpha}(J^{S}_{x})^{\alpha\beta} U_{\beta l}$. Note that we dropped the diagonal terms $l=m$ in the summations in Eqs. (16) and (17) since they vanish identically. We also note that the transformation from the first row to the second row in Eq. (16) was performed since $\Sigma_{l,m}\mathrm{Re}\{(J^{S}_{x})^{ml}(J^{C}_{y})^{lm}\}$ identically vanishes after $\boldsymbol{k}$ summation. After performing the ω integration in Eq. (17), the Fermi sea term is given by $\sigma^{zII}_{xy} = \sigma^{zIIa}_{xy} + \sigma^{zIIb}_{xy}$, where

$$\sigma_{xy}^{zIIa} = \frac{-1}{2\pi N}\sum_{\boldsymbol{k},l\neq m} \mathrm{Im}\{(J_x^S)^{ml}(J_y^C)^{lm}\}\frac{1}{E_{\boldsymbol{k}}^l - E_{\boldsymbol{k}}^m} \times \mathrm{Im}\left\{\frac{E_{\boldsymbol{k}}^l + E_{\boldsymbol{k}}^m - 2i\gamma}{(E_{\boldsymbol{k}}^l - i\gamma)(E_{\boldsymbol{k}}^m - i\gamma)}\right\}, \quad (18)$$

$$\sigma_{xy}^{zIIb} = \frac{1}{\pi N}\sum_{\boldsymbol{k},l\neq m} \mathrm{Im}\{(J_x^S)^{ml}(J_y^C)^{lm}\}\frac{1}{(E_{\boldsymbol{k}}^l - E_{\boldsymbol{k}}^m)^2} \times \mathrm{Im}\left\{\ln\left(\frac{E_{\boldsymbol{k}}^l - i\gamma}{E_{\boldsymbol{k}}^m - i\gamma}\right)\right\}. \quad (19)$$

Here, we used the following relation to perform the ω integration:

$$\int_{-\infty}^{\mu} dx\left\{\frac{1}{(x-a)^2(x-b)} - \frac{1}{(x-a)(x-b)^2}\right\} = \frac{a+b-2\mu}{(a-b)(a-\mu)(b-\mu)} - \frac{2}{(a-b)^2}\ln\left(\frac{a-\mu}{b-\mu}\right). \quad (20)$$

In the case of $\gamma\to 0$, σ_{xy}^{zIIb} given by Eq. (19) corresponds to the Berry curvature term as follows:

$$\sigma_{xy}^{zIIb} = \frac{1}{N}\sum_{\boldsymbol{k},l} f(E_{\boldsymbol{k}}^l)\Omega^l(\boldsymbol{k}), \quad (21)$$

where $\Omega^l(\boldsymbol{k})$ represents the Berry curvature given by

$$\Omega^l(\boldsymbol{k}) = \sum_{m\neq l}\frac{2\,\mathrm{Im}\{(J_x^S)^{ml}(J_y^C)^{lm}\}}{(E_{\boldsymbol{k}}^l - E_{\boldsymbol{k}}^m)^2}. \quad (22)$$

The relation $\sigma_{xy}^z = \sigma_{xy}^{zIIb}$ has been frequently assumed in literatures such as Ref. 9 In this study, we calculate all the Fermi surface and Fermi sea terms correctly, and we elucidate how each term contributes to the SHC and OHC. In Sec. V B, we will discuss the γ dependences of $\sigma_{xy}^{zI}, \sigma_{xy}^{zIIa}$, and σ_{xy}^{zIIb} in detail.

B. Discussion on the current vortex correction

In Sec. III A, we have neglected the CVC. Here, we calculate the CVC due to the local impurity potential in the Born approximation and show that it is negligible in transition metals. In the Born approximation, the lowest order CVC is given by

$$\Delta\hat{J}_\mu^C = \frac{1}{N}n_{imp}I^2\sum_{\boldsymbol{k}}\hat{G}^R\hat{J}_\mu^C\hat{G}^A. \quad (23)$$

Its diagrammatic expression is given in Fig. 2. The magnitude of CVC depends on the model. For example, the CVC identically vanishes in the d-orbital tight-binding models with atomic SOI.[7,22] In contrast, the CVC plays an essential role in a Rashba model: the SHC vanishes due to the cancellation by CVC.[23]

Here, we study the CVC in fcc and bcc transition metals, where each atomic site is a center of inversion symmetry. The s- and d-orbital atomic wave functions have an even parity with respect to $\boldsymbol{k}\to-\boldsymbol{k}$, whereas the p-orbital atomic wave functions have an odd parity. Therefore, the Hamiltonian for a fcc metal and that for a bcc metal has the following relationship:

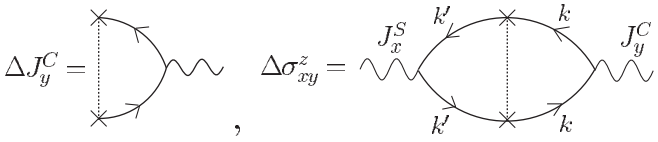

FIG. 2. The diagrammatic expressions of the current vertex correction due to the local impurity potentials. Here, the diagram represents the lowest order correction to the current $\Delta\hat{J}_x^C$ and spin Hall conductivity $\Delta\sigma_{xy}^z$.

$$(H_0(\boldsymbol{k}))_{\alpha\beta} = p(H_0(-\boldsymbol{k}))_{\alpha\beta}, \quad (24)$$

where $p=-1$ only when either α or β is a p orbital, otherwise $p=1$. It is easy to show that $(G(\boldsymbol{k},\omega))_{\alpha\beta}$ has the same parity as $(H_0(\boldsymbol{k}))_{\alpha\beta}$. Therefore, when both α and β are (s,d) orbitals, $(\Delta\hat{J}_\mu^C)_{\alpha\beta}=0$ since the (α,β) components of $(\partial/\partial k_\mu)\hat{G} = \hat{G}\hat{J}_\mu^C\hat{G}$ are odd functions. On the other hand, $(\Delta\hat{J}_\mu^C)_{\alpha\beta}\neq 0$ when either α or β is a p orbital since $(\partial\hat{G}/\partial k_\mu)_{\alpha\beta}$ is an even function. Although $(\Delta\hat{J}_\mu^C)_{\alpha\beta}$ originating from the p orbital is finite, it is small in magnitude since the $5p$ and $6p$ levels are about 20 eV higher than the Fermi level μ and the p-electron density of states (DOS) at μ is very small in all transition metals.

Now, let us numerically verify that the contribution of CVC to SHC is small in magnitude. The correction to the SHC due to the lowest order CVC is given by

$$\Delta\sigma_{xy}^z = \frac{1}{2\pi N^2}n_{imp}I^2\sum_{\boldsymbol{k},\boldsymbol{k}'}\mathrm{Tr}[\hat{J}_x^S\hat{G}_{\boldsymbol{k}'}^R\Delta\hat{J}_y^C\hat{G}_{\boldsymbol{k}'}^A] = \frac{1}{2\pi N^2}n_{imp}I^2\sum_{\boldsymbol{k},\boldsymbol{k}'}\mathrm{Tr}[\hat{G}_{\boldsymbol{k}'}^A\hat{J}_x^S\hat{G}_{\boldsymbol{k}'}^R\hat{G}_{\boldsymbol{k}}^R\hat{J}_y^C\hat{G}_{\boldsymbol{k}}^A]. \quad (25)$$

Its diagrammatic expression is given in Fig. 2. We numerically calculated $\Delta\sigma_{xy}^z$ and found that it is very small as compared to σ_{xy}^z without CVC: the ratio $|\Delta\sigma_{xy}^z|/|\sigma_{xy}^z|$ is $\sim$0.02 for Ta and Pt, and $\sim$0.005 for W when γ=0.002–0.02. The ratio is independent of γ because of the following reason: Since $\Sigma_{\boldsymbol{k}}G_{\boldsymbol{k}}^RG_{\boldsymbol{k}}^A\sim O(\gamma^{-1})$, and $\gamma\propto n_{imp}I^2$, ΔJ_μ^C in Eq. (23) is independent of γ. In the present model, the higher order correction to the SHC should be negligible.

In the case of hcp transition metals, $(\Delta\hat{J}_\mu^C)_{\alpha\beta}\neq 0$ even when α and β are (s,d) orbitals, since each atomic site is not a center of inversion symmetry. To find out the importance of the CVC in hcp metals, we performed the numerical calculation for Os and found out that the ratio $|\Delta\sigma_{xy}^z|/|\sigma_{xy}^z|$ is $\sim$0.06 in Os in the low resistive regime. Although it is much larger than that in Pt, Ta, and W, the CVC is qualitatively negligible even in hcp transition metals. Therefore, we are allowed to neglect the CVC even for hcp transition metals.

C. Spin Hall conductivity and orbital Hall conductivity considering the overlap integrals between different sites

In the previous section, we studied the SHC and OHC under the assumption that the atomic wave functions of different sites are orthogonal. However, for a more accurate quantitative study of the intrinsic SHE and OHE, we need to take the off-diagonal elements of $O_{\alpha\beta}$ in Eq. (5) into account correctly. In this section, we explain how to calculate the SHE and OHE when the overlap integrals between different sites are considered.

Here, we introduce the Bloch wave function, which is given by

$$\phi_{\boldsymbol{k}\alpha}(\boldsymbol{r}) = \frac{1}{\sqrt{N}}\sum_i e^{i\boldsymbol{k}\cdot\boldsymbol{R}_i}\phi_\alpha(\boldsymbol{r}-\boldsymbol{R}_i). \tag{26}$$

In this case, the inner product between the Bloch wave functions with different $\boldsymbol{k}$ and α is given by

$$\int d\boldsymbol{r}\,\phi^*_{\boldsymbol{k}\alpha}(\boldsymbol{r})\,\phi_{\boldsymbol{k}'\beta}(\boldsymbol{r}) = \delta_{\boldsymbol{k}\boldsymbol{k}'}O_{\alpha\beta}(\boldsymbol{k}), \tag{27}$$

where

$$O_{\alpha\beta}(\boldsymbol{k}) = \sum_i e^{-i\boldsymbol{k}\cdot\boldsymbol{R}_i}O_{\alpha\beta}(\boldsymbol{R}_i). \tag{28}$$

Here, $O_{\alpha\beta}(\boldsymbol{R}_i)$ in Eq. (28) is the overlap integral defined by Eq. (5). Therefore, when the overlap integrals between different sites are considered, the Bloch wave function given by Eq. (26) is nonorthogonal.

By including the chemical potential μ, the kinetic term of the Hamiltonian is given by[49]

$$\hat{H}_0 = \sum_{\boldsymbol{k},\alpha,\beta} c^\dagger_{\boldsymbol{k}\alpha}[h_{\alpha\beta}(\boldsymbol{k}) - \mu O_{\alpha\beta}(\boldsymbol{k})]c_{\boldsymbol{k}\beta}, \tag{29}$$

where $c_{\boldsymbol{k}\alpha}$ is defined by

$$c_{\boldsymbol{k}\alpha} = \frac{1}{\sqrt{N}}\sum_i e^{i\boldsymbol{k}\cdot\boldsymbol{R}_i}c_{i\alpha}. \tag{30}$$

Here, $c_{i\alpha}$ is an annihilation operator of an electron in the α orbital state at the ith site. As the atomic wave functions at different sites are nonorthogonal, creation and annihilation operators $c^\dagger_{\boldsymbol{k}\alpha}$, and $c_{\boldsymbol{k}\alpha}$ do not satisfy the canonical anticommutation relations but, instead, satisfy[49]

$$\{c_{\boldsymbol{k}\alpha}, c^\dagger_{\boldsymbol{k}'\beta}\} = \delta_{\boldsymbol{k}\boldsymbol{k}'}O^{-1}_{\alpha\beta}(\boldsymbol{k}). \tag{31}$$

Since matrix $\hat{O}(\boldsymbol{k})$ is a positive definite Hermitian matrix, we can introduce the following matrix $\hat{S}(\boldsymbol{k})$ that transforms $\hat{O}(\boldsymbol{k})$ into the unit matrix 1:

$$\hat{S}^\dagger(\boldsymbol{k})\hat{O}(\boldsymbol{k})\hat{S}(\boldsymbol{k}) = 1. \tag{32}$$

We note that matrix $\hat{S}(\boldsymbol{k})$ cannot be determined uniquely: By using an arbitrary unitary matrix $\hat{X}$, $\hat{S}=\hat{S}\hat{X}$ also satisfies Eq. (32). Here, we introduce the following new basis $(\bar{c}_{\boldsymbol{k}\alpha}, \bar{c}^\dagger_{\boldsymbol{k}\alpha})$ using $\hat{S}(\boldsymbol{k})$:

$$\bar{c}_{\boldsymbol{k}\alpha} = \sum_\beta S^{-1}_{\alpha\beta}(\boldsymbol{k})c_{\boldsymbol{k}\beta}. \tag{33}$$

We can easily verify that these operators $(\bar{c}_{\mathbf{k}\alpha}, \bar{c}^\dagger_{\mathbf{k}\alpha})$ satisfy the canonical anticommutation relations $\{\bar{c}_{\boldsymbol{k}\alpha}, \bar{c}^\dagger_{\boldsymbol{k}'\beta}\} = \delta_{\boldsymbol{k}\boldsymbol{k}'}\delta_{\alpha\beta}$. In this basis, Eq. (29) is rewritten as

$$\hat{H}_0 = \sum_{\boldsymbol{k},\alpha,\beta} \bar{c}^\dagger_{\boldsymbol{k}\alpha}[\bar{h}_{\alpha\beta}(\boldsymbol{k}) - \mu\delta_{\alpha\beta}]\bar{c}_{\boldsymbol{k}\beta}, \tag{34}$$

where $\bar{h}_{\alpha\beta}(\boldsymbol{k}) = (\hat{S}^\dagger(\boldsymbol{k})\hat{h}(\boldsymbol{k})\hat{S}(\boldsymbol{k}))^{\alpha\beta} \equiv (\hat{\bar{h}}(\boldsymbol{k}))^{\alpha\beta}$. Therefore, the Green function in the $(\bar{c}_{\boldsymbol{k}\alpha}, \bar{c}^\dagger_{\boldsymbol{k}\alpha})$ basis is given by

$$\hat{\bar{G}}(\boldsymbol{k},\omega) = [\omega + \mu - \hat{\bar{h}}(\boldsymbol{k})]^{-1}. \tag{35}$$

Next, we derive the expression for the current operator in the $(c_{\boldsymbol{k}\alpha}, c^\dagger_{\boldsymbol{k}\alpha})$ basis. From the continuity equation $\frac{\partial}{\partial t}n(\boldsymbol{r}) + \nabla\cdot\boldsymbol{j}(\boldsymbol{r}) = 0$, we obtain

$$\frac{\partial}{\partial t}n(\boldsymbol{q}) = -i\boldsymbol{q}\cdot\boldsymbol{j}(\boldsymbol{q}), \tag{36}$$

where n is the electron number density. $\frac{\partial}{\partial t}n(\boldsymbol{q})$ can be calculated by the equation of motion as $\frac{\partial}{\partial t}n(\boldsymbol{q}) = i[H, n(\boldsymbol{q})]$. Therefore, the x component of the current operator j_x is given by

$$j_x = \lim_{q_x\to 0}\left(-\frac{1}{q_x}[H, n(\boldsymbol{q})]\right). \tag{37}$$

In Appendix A, we will show that $n(\boldsymbol{q})$ is given by

$$n(\boldsymbol{q}) = \sum_{\boldsymbol{k},\alpha,\beta} O^{-1}_{\alpha\beta}(\boldsymbol{k})c^\dagger_{\boldsymbol{k}-(\boldsymbol{q}/2),\alpha}c_{\boldsymbol{k}+(\boldsymbol{q}/2),\beta}, \tag{38}$$

which is an exact expression for the first order of $|\boldsymbol{q}|$. By using the following relationship: $[AB, CD] = A\{B, C\}D - AC\{B, D\} + \{A, C\}DB - C\{A, D\}B$, $[H, n(\boldsymbol{q})]$ is given by

$$[H, n(\boldsymbol{q})] = \sum_{\boldsymbol{k},\alpha,\beta} c^\dagger_{\boldsymbol{k}-(\boldsymbol{q}/2),\alpha}(\{\hat{h}[\boldsymbol{k}-(\boldsymbol{q}/2)]\hat{O}^{-1}[\boldsymbol{k}-(\boldsymbol{q}/2)]\hat{O}(\boldsymbol{k})\}^{\alpha\beta} - \{\hat{O}(\boldsymbol{k})\hat{O}^{-1}[\boldsymbol{k}+(\boldsymbol{q}/2)]\hat{h}[\boldsymbol{k}+(\boldsymbol{q}/2)]\}^{\alpha\beta})c_{\boldsymbol{k}+(\boldsymbol{q}/2),\beta}. \tag{39}$$

By substituting Eq. (39) into Eq. (37), we obtain the expression for the velocity in the $(c_{\boldsymbol{k}\alpha}, c^\dagger_{\boldsymbol{k}\alpha})$ basis as follows:

$$\hat{v}_x(\boldsymbol{k}) = \frac{\partial\hat{h}(\boldsymbol{k})}{\partial k_x} + \frac{1}{2}\hat{h}(\boldsymbol{k})\hat{D}_x(\boldsymbol{k}) + \frac{1}{2}\hat{D}^\dagger_x(\boldsymbol{k})\hat{h}(\boldsymbol{k}), \tag{40}$$

where $D_x(\boldsymbol{k})$ is given by

$$\hat{D}_x(\boldsymbol{k}) = \left\{\frac{\partial}{\partial k_x}\hat{O}^{-1}(\boldsymbol{k})\right\}\hat{O}(\boldsymbol{k}) = -\hat{O}^{-1}(\boldsymbol{k})\frac{\partial}{\partial k_x}\hat{O}(\boldsymbol{k}). \tag{41}$$

Apparently, $\hat{D}_x(\boldsymbol{k}) = 0$ in an orthogonal basis. We call the second and third terms in Eq. (40) the overlap integral current. In the $(\bar{c}_{\boldsymbol{k}\alpha}, \bar{c}^\dagger_{\boldsymbol{k}\alpha})$ basis, the velocity $\hat{\bar{v}}_x(\boldsymbol{k})$ is given by

$$\hat{\bar{v}}_x(\boldsymbol{k}) = \hat{S}^\dagger(\boldsymbol{k})\hat{\bar{v}}_x(\boldsymbol{k})\hat{S}(\boldsymbol{k}). \tag{42}$$

Therefore, even when the overlap integrals between different sites exist, we can calculate the SHC and OHC in the basis

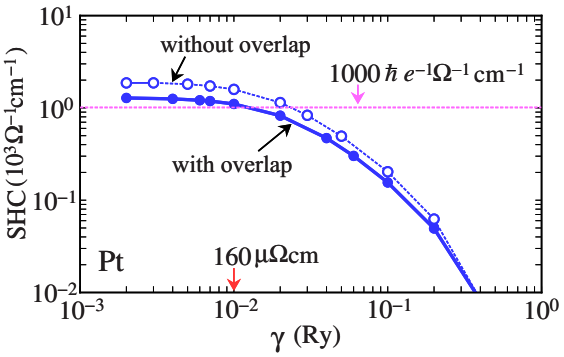

FIG. 3. (Color online) γ dependence of SHC in Pt obtained by using Eq. (5) (with overlap) and Eq. (6) (without overlap). When the overlap integrals between different sites are considered, the magnitude of SHC is reduced by about half. The resistivity that corresponds to $\gamma=0.01$ is $\sim 160\ \mu\Omega$ cm in Pt.

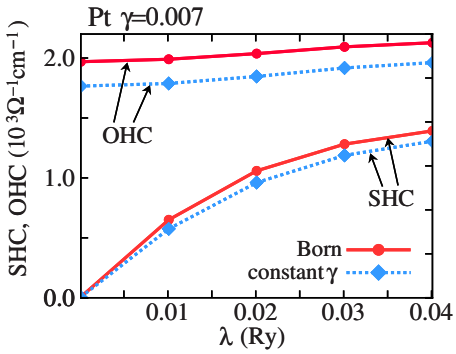

FIG. 4. (Color online) λ dependence of SHC and OHC in Pt given by the Born approximation and the constant γ approximation. The SHCs obtained in these two approximations give quantitatively similar results. We stress that the OHC is finite even if $\lambda=0$.

$(\bar{c}_{\boldsymbol{k}\alpha},\bar{c}^{\dagger}_{\boldsymbol{k}\alpha})$ by using the matrix $\hat{S}(\boldsymbol{k})$. In this basis, the Green function $\hat{\bar{G}}(\boldsymbol{k},\omega)$ is given by Eq. (35). The charge current operator $\hat{\bar{J}}^C_\mu$ and the spin current operator $\hat{\bar{J}}^S_\mu$ are given by

$$\hat{\bar{J}}^C_\mu=\begin{pmatrix}\bar{v}_\mu & 0\\ 0 & \bar{v}_\mu\end{pmatrix},\quad \hat{\bar{J}}^S_\mu=\begin{pmatrix}\bar{v}_\mu & 0\\ 0 & -\bar{v}_\mu\end{pmatrix}. \tag{43}$$

Also, the l_z-orbital current is given by $\hat{\bar{J}}^O_\mu=\{\hat{\bar{J}}^C_\mu,\hat{\bar{l}}_z\}/2$, where $\hat{\bar{l}}_z=\hat{S}^{\dagger}(\boldsymbol{k})\hat{l}_z\hat{S}(\boldsymbol{k})$. Therefore, SHC and OHC can be calculated by substituting $\hat{G}(\boldsymbol{k},\omega),\hat{J}^C_\mu$, and $\hat{J}^S_\mu$ in Eqs. (13) and (14) with $\hat{\bar{G}}(\boldsymbol{k},\omega)$, $\hat{\bar{J}}^C_\mu$, and $\hat{\bar{J}}^S_\mu$, respectively.

Figure 3 shows the obtained SHCs in Pt by considering the overlap integrals between different sites in the NRL-TB model. For comparison, SHC given by using Eq. (6) is also shown. We find that the magnitude of the SHC is reduced by about half when the overlap integral is considered correctly. We have verified that this is mainly due to the changes of the band spectra, whereas the modification due to the overlap integral current, which is given by the second and third terms in Eq. (40), is less than 10% in magnitude. Since the CVC is also little affected by the modification of the velocity, we can also safely neglect the CVC when the overlap integrals between different sites are considered.

Here, we comment on the previous study in Ref. 8 Therein, the SHC in Pt using Eq. (6) was reported. Since the Fermi surface is mainly composed of d electrons in Pt and the d-orbital atomic wave functions are well localized, the band structure near the Fermi level is described well in this approximation. Therefore, the calculations of SHC and OHC in the absence of the overlap integrals between different sites give semiquantitatively reliable results, which can be recognized from Fig. 3.

IV. NUMERICAL STUDY

A. Numerical results for spin Hall conductivity and orbital Hall conductivity

In this section, we perform the numerical calculations for the SHC and OHC in various $4d$ and $5d$ transition metals by considering the overlap integrals between different sites given by Eq. (5). In particular, we clarify SOI (λ), the quasiparticle damping rate (γ), and the chemical potential (μ) dependences of the SHC and OHC in each metal. Here, we note that the units of the SHC and OHC are $|e|/2\pi a$ and $1[|e|/2\pi a]\approx 1000\ \hbar e^{-1}\ \Omega^{-1}\ \mathrm{cm}^{-1}$ for $a=4$ Å.

First, we discuss the quasiparticle damping rate $\hat{\Gamma}$ dependence of SHC. In the Born approximation, $\hat{\Gamma}$ depends on orbital index. When $\lambda \ll W_{band}$, $\hat{\Gamma}$ is diagonal with respect to the orbital: $\Gamma_{\alpha\beta}=\gamma_\alpha\delta_{\alpha\beta}$, where $\gamma_\alpha \propto \rho_\alpha(0)$. On the other hand, the quasiparticle damping rate γ_α is independent of the orbital in the constant γ approximation: $\Gamma_{\alpha\beta}=\gamma\delta_{\alpha\beta}$. In Fig. 4, the SHCs for $\gamma=0.007$ in these two approximations are shown. We see that the obtained SHC is quantitatively similar in both approximations. This fact can be explained as follows: In transition metals, the LDOS of t_{2g}-(d_{xy},d_{yz},d_{zx}) and e_g-$(d_{x^2-y^2},d_{3z^2-r^2})$ orbitals are almost equal in magnitude. Since $\gamma_\alpha \propto \rho_\alpha(0)$ in the Born approximation, two approximation give similar results in transition metals. For this reason, we use the constant γ approximation hereafter. In contrast, the SHC in Sr_2RuO_4 given by the Born approximation is much larger than that given by the constant γ approximation since the α dependence of ρ_α is large.[7]

Figure 4 also shows the OHCs in these two approximations. As already pointed out in Refs. 7 and 8, a huge OHC appears even if $\lambda=0$, and it slowly increases with λ. In Sr_2RuO_4, in contrast, the OHC slowly decreases with λ.[7]

Figure 5 shows the electron number n dependence of the SHC, where $n=n_s+n_d$. Note that the crystal structure of various transition metals is shown in Table I. The SHC obtained in the present model for $\gamma=0.002$ is shown in Fig. 5(a), and for $\gamma=0.02$ and 0.2 in Fig. 5(b). The SHC is negative for $n=5$ and 6, and positive for $n=9-11$: The SHC changes its sign at around $n=7$ and 8. The magnitude of SHC is largest in Pt for $\gamma=0.002$ and 0.02, where the corresponding resistivities are ~ 8 and $\sim 64\ \mu\Omega$ cm in Pt, respectively. When $\gamma=0.2$, however, the absolute values of SHCs in Ta and W become larger than that in Pt, where $\rho\sim 220\ (250)\ \mu\Omega$ cm in Pt (Ta and W). Therefore, large negative values of SHCs in Ta and W will be observed even in high resistive samples. For comparison, we also calculated the SHC for $n=5-9$ by

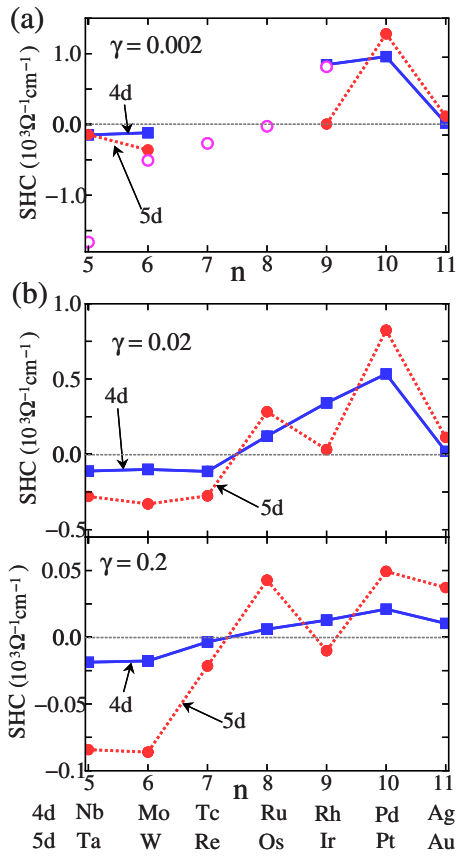

FIG. 5. (Color online) n dependence of SHC for γ=0.002, 0.02, and 0.2. In (a), we see that Pt shows the largest SHC for γ=0.002. The open symbols represents the SHC in Pt for n=5–9. In (b), the SHCs obtained in the present model for n=7 and 8 (hcp structure) are also shown. SHC in W takes the largest value for γ=0.2.

using the band structure of Pt, which is represented by the open symbols in Fig. 5(a). We see that the magnitude of SHC in Pt with n=9 does not reproduce that in Ir. The same is true in Ta and W (bcc structure). Therefore, we need to calculate SHC using a correct band structure for each metal.

Next, we examine the λ dependence of the SHC. We verified that the SHC in each metal increases approximately proportional to λ as shown in Fig. 4. To elucidate the origin of SHC, we calculated the SHC when SOI is anisotropic: $\lambda_1\Sigma(\hat{l}_z\hat{s}_z)+\lambda_2\Sigma(\hat{l}_x\hat{s}_x+\hat{l}_y\hat{s}_y)$. We find that the SHC for $H_{SO}=\lambda\Sigma(\hat{l}_z\hat{s}_z)(\lambda_1=\lambda,\lambda_2=0)$ is as large as the SHC in the isotropic case ($\lambda_1=\lambda_2=\lambda$). In contrast, the SHC for $H_{SO}=\lambda\Sigma(\hat{l}_x\hat{s}_x+\hat{l}_y\hat{s}_y)(\lambda_1=0,\lambda_2=\lambda)$ is 1 order of magnitude smaller than the isotropic case. Therefore, the z component of the SOI gives the decisive contribution to the SHC. The matrix element of $\hat{l}_z$ is finite only for $\langle yz|l_z|zx\rangle=-\langle zx|l_z|yz\rangle=i$ and $\langle xy|l_z|x^2-y^2\rangle=-\langle x^2-y^2|l_z|xy\rangle=2i$. Note that d_{xy} and $d_{x^2-y^2}$ orbitals (d_{yz} and d_{zx} orbitals) are given by the linear combination of $l_z=\pm2(l_z=\pm1)$. Here, we examine which orbitals cause a significant contribution to the SHC. The z component of SOI is rewritten as $\lambda_3\Sigma_i\{P(l_z^2=1)(\hat{l}_z\hat{s}_z)\}_i+\lambda_4\Sigma_i\{P(l_z^2=4)(\hat{l}_z\hat{s}_z)\}_i$, where $P(l_z^2=n)$ represents the projection operator. SHC caused by d_{xy} and $d_{x^2-y^2}$ orbitals is given by setting $\lambda_3=0$ and $\lambda_4=\lambda$ which are represented as $l_z=\pm2$ in Table II. Similarly, SHC caused d_{yz} and d_{zx} orbitals is given by setting $\lambda_3=\lambda$ and $\lambda_4=0$, which are represented as $l_z=\pm1$ in Table II. We see that the interorbital transition between d_{xy} and $d_{x^2-y^2}$ orbitals causes a significant contribution to the SHC in many metals. Only in the case of Mo, W, and Ir, the contribution of d_{zx} and d_{yz} orbitals is comparable to that of d_{xy} and $d_{x^2-y^2}$ orbitals. In other metals, d_{xy} and $d_{x^2-y^2}$ orbitals give the dominant contribution to the SHC.

TABLE II. SHC that originates from the d_{zx}, d_{yz}, d_{xy}, and $d_{x^2-y^2}$ orbitals. Here, we set γ=0.02. $l_z=\pm2$ ($l_z=\pm1$) represents the SHC caused by d_{xy} and $d_{x^2-y^2}$ orbitals (d_{yz} and d_{zx} orbitals). The ratio represents (SHC from $l_z=\pm2$)/(SHC from $l_z=\pm1$). We see that d_{xy} and $d_{x^2-y^2}$ orbitals cause a significant contribution to the SHC in many metals.

Metals	$l_z=\pm1$	$l_z=\pm2$	Ratio
Nb($4d^45s^1$)	−0.0332	−0.0770	2.32
Mo($4d^55s^1$)	−0.0474	−0.0587	1.24
Rh($4d^85s^1$)	0.0847	0.269	3.18
Pd($4d^{10}5s^0$)	0.0847	0.455	5.37
Ag($4d^{10}5s^1$)	0.00224	0.0181	8.08
Ta($5d^36s^2$)	−0.0222	−0.254	11.4
W($5d^46s^2$)	−0.174	−0.205	1.18
Ir($5d^96s^0$)	0.0123	0.0231	1.89
Pt($5d^96s^1$)	0.136	0.678	4.98
Au($5d^{10}6s^1$)	0.0177	0.0987	5.59

Here, we show the OHCs for γ=0.02 in various transition metals in Fig. 6. We see that all the 4d and 5d transition metals show huge and positive OHCs, which are almost 1 order of magnitude larger than the SHCs. In Au (Ag), the OHC takes a small value since the d-electron DOS is small at the Fermi level. Therefore, a huge and positive OHC is a universal nature of transition metals. As in the case of the SHE, the intrinsic OHE shows the crossover behavior: the OHC is independent of ρ in the low resistive regime, whereas it decreases in proportion to ρ^{-2} in the high resistive regime.[7,8] In a later publication, we will present an intuitive (semiclassical) explanation of the origin of the OHC.[34]

Now, we discuss the γ dependences of SHC and OHC. The γ dependence of intrinsic SHCs in Ta and W are shown

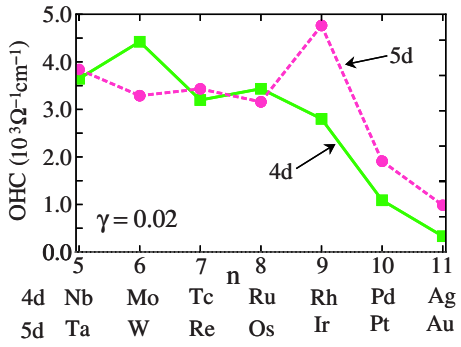

FIG. 6. (Color online) n dependence of OHC for γ=0.02. The obtained OHCs are positive for all metals, and they are about ten times larger than the SHCs except for Pt and Pd.

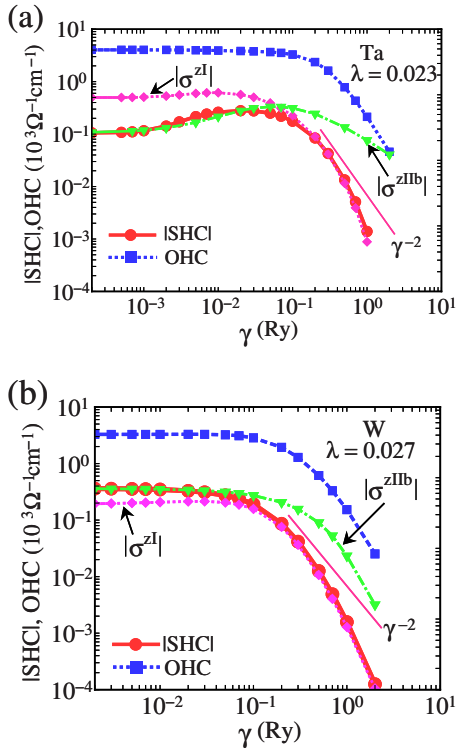

FIG. 7. (Color online) γ dependence of SHC and OHC in (a) Ta and (b) W. The corresponding resistivity ρ to γ=0.1 is ~190 $\mu\Omega$ cm in Ta and ~220 $\mu\Omega$ cm in W.

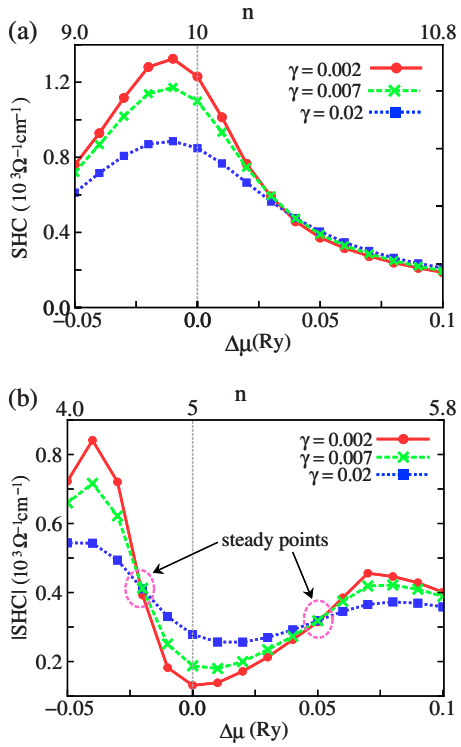

FIG. 8. (Color online) μ dependence of σ_{xy}^{zIIb} in (a) Pt and (b) Ta for γ=0.002, 0.007, and 0.02. The chemical potential is given by $\mu=\mu_0+\Delta\mu$, where μ_0 represents the true value of the chemical potential. Total electron number n is shown in the upper horizontal axis. Note that the sign of the SHC in Ta is negative.

in Fig. 7. Usually, the intrinsic Hall conductivities are independent of γ in the low resistive regime where $\gamma \ll \Delta$, whereas it decreases approximately proportional to ρ^{-2} in the high resistive regime where $\Delta \ll \gamma$.[15,22] Here, Δ represents the band splitting measured from the Fermi level. In W, Δ is ~0.04, and in Pt, Δ is ~0.035.[8] We find that W shows a typical coherent-incoherent crossover at $\gamma \sim \Delta$ in Fig. 7(b). We have also verified that the coherent-incoherent crossover behavior is universally seen in many transition metals including Pt, which is shown in Fig. 3(a). However, as shown in Fig. 7(a), SHC in Ta shows an exceptional behavior: It takes a maximum value at around $\gamma \sim 0.02$ and decreases as γ decreases in the low resistive regime. We find that this anomalous behavior can arise when almost degenerate anticrossing points exist slightly away from the Fermi level. We will discuss the reason in detail in Sec. IV B.

In Fig. 7(b), the γ dependences of the Fermi surface term σ_{xy}^{zI} and the Fermi sea terms σ_{xy}^{zIIa},σ_{xy}^{zIIb} are also shown. In the low resistive regime, the relation $\sigma_{xy}^{zI} \simeq \sigma_{xy}^{zIIb}$ holds well, and σ_{xy}^{zIIb} reproduces the total Hall conductivity σ_{xy}^{z}.[5] In the high resistive regime, however, $\sigma_{xy}^{z} \simeq \sigma_{xy}^{zI}$, whereas σ_{xy}^{z} is quite different from σ_{xy}^{zIIb} in the high resistive regime. As a result, the relationship

$$\sigma_{xy}^{z} \simeq \sigma_{xy}^{zI} \quad \text{(Fermi surface term)} \tag{44}$$

is recognized for a wide range of γ. We will discuss the crossover behavior of the intrinsic Hall conductivity in more detail in Sec. V B.

We also discuss the γ dependence of OHC. The obtained OHCs in Ta and W are shown in Fig. 7. The coherent-incoherent crossover behavior of OHC is recognized in Fig. 7. In contrast to the γ dependence of SHC in Ta, OHC shows a typical crossover behavior. We also verified that OHC is finite even if λ=0 since the d-orbital current in Eq. (12) is independent of the spin index.[7]

Now, we discuss the μ dependence of SHC in Pt and Ta by assuming that the band structure is rigid. Experimentally, the chemical potential μ can be controlled by composing alloys. Figure 8(a) shows the μ dependence of σ_{xy}^{zIIb} in Pt for γ=0.002, 0.007, and 0.02. Here, the chemical potential is given by $\mu=\mu_0+\Delta\mu$, where μ_0 represents the true value of the chemical potential. We see that the SHC shows a peak at around $\Delta\mu$=0, and it decreases when μ is raised or lowered from its true value. This $\Delta\mu$ dependence of SHC obtained in the present model in Pt seems to be in good agreement with that in Ref. 9. We see that SHC for γ=0.002 is about 45% larger than that for γ=0.02 at $\Delta\mu$=0.

Here, we elucidate from which part of the surface the SHC in Pt originates by calculating

$$\sigma_{xy}^{z}(\boldsymbol{k}) \equiv \frac{1}{8} \sum_{k_x',k_y',k_z'}^{(\pm k_x,\pm k_y,\pm k_z)} \mathrm{Tr}[\hat{J}_x^S \hat{G}^R \hat{J}_y^C \hat{G}^A]_{\boldsymbol{k}',\omega=0}.$$

Note that $\frac{1}{2\pi N}\Sigma_{\boldsymbol{k}}\sigma_{xy}^{z}(\boldsymbol{k})$ is equal to Eq. (13). $\sigma_{xy}^{z}(\boldsymbol{k})$ is finite only on the Fermi surface, and it takes a huge value at

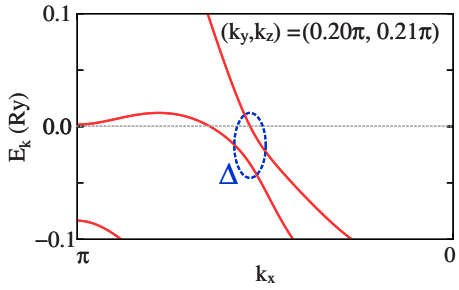

FIG. 9. (Color online) The k_x dependence of $E_{\boldsymbol{k}}^l$ for $(k_y,k_z)=(0.20\pi,0.21\pi)$ in Pt is shown. The band splitting measured from the Fermi level is $\Delta\sim 0.035$. A wide area at around $(k_x,k_y,k_z)=(0.54\pi,0.20\pi,0.21\pi)$ gives a dominant contribution to SHC in Pt.

$(0.76\pi,0,0)$ (on Γ-X) and at $(0.44\pi,0.44\pi,0.44\pi)$ (on L-Γ) since two bands are very close near the Fermi level in the present model:[8] $\sigma_{xy}^z(\boldsymbol{k})\sim 3000$ for the former point and $\sigma_{xy}^z(\boldsymbol{k})\sim 5000$ for the latter point in the present model. However, the contribution of these points to the SHC is small after taking $\boldsymbol{k}$ summation using 512^3 $\boldsymbol{k}$ meshes. We verified that the dominant contribution comes from a wide area around $(k_x,k_y,k_z)=(0.54\pi,0.20\pi,0.21\pi)$, as shown in Fig. 9.

Figure 8(b) shows the μ dependence of σ_{xy}^{zIIb} in Ta for $\gamma=0.002$, 0.007, and 0.02. In Ta, several "steady points," where the magnitude of SHC is approximately independent of γ in the low resistive regime, are recognized at $\Delta\mu=-0.02$ and at $\Delta\mu=+0.05$ in Fig. 8(b). When μ decreases across the steady point at $\Delta\mu=-0.02$, the magnitude of SHC increases and reaches a peak at around $\Delta\mu=-0.04$. This peak originates from the almost degenerate anticrossing bands, which are discussed in more detail in Sec. IV B.

Finally, we explain why SHC in Ir is small in magnitude by analyzing $\Sigma_{\boldsymbol{k}}\sigma_{xy}^z(\boldsymbol{k})$. Here, we divide the $\boldsymbol{k}$ summation into the $\boldsymbol{k}^+$ and $\boldsymbol{k}^-$ regions, where the $\boldsymbol{k}^+$ region ($\boldsymbol{k}^-$ region) represents the region where $\sigma_{xy}^z(\boldsymbol{k})>0[\sigma_{xy}^z(\boldsymbol{k})<0]$ holds:

$$\sum_{\boldsymbol{k}}\sigma_{xy}^z(\boldsymbol{k})=\sum_{\boldsymbol{k}^+}\sigma_{xy}^z(\boldsymbol{k})+\sum_{\boldsymbol{k}^-}\sigma_{xy}^z(\boldsymbol{k})\equiv\sigma_{xy}^{z+}+\sigma_{xy}^{z-}. \quad (45)$$

In many transition metals, such as Pt and Ta, either σ_{xy}^{z+} or $|\sigma_{xy}^{z-}|$ is much larger than the other. In Ir, however, we have verified that the relation $\sigma_{xy}^{z+}\simeq|\sigma_{xy}^{z-}|$ holds and, therefore, σ_{xy}^z becomes small in magnitude.

B. Mechanism of impurity-assisted spin Hall conductivity

In the previous section, we have verified that the SHC in all $4d$ and $5d$ transition metals except for Ta are independent of γ in the low resistive regime ($\gamma\ll\Delta$). Here, we show that the SHC can show a nonmonotonic γ dependence in the low resistive regime when almost degenerate anticrossing points exist slightly away from the Fermi level, because of the impurity-assisted interband excitation. This is the origin of the anomalous γ dependence of the SHC in Ta for $\gamma<0.02$ in Fig. 7(a). We call this phenomenon the impurity-assisted SHE.

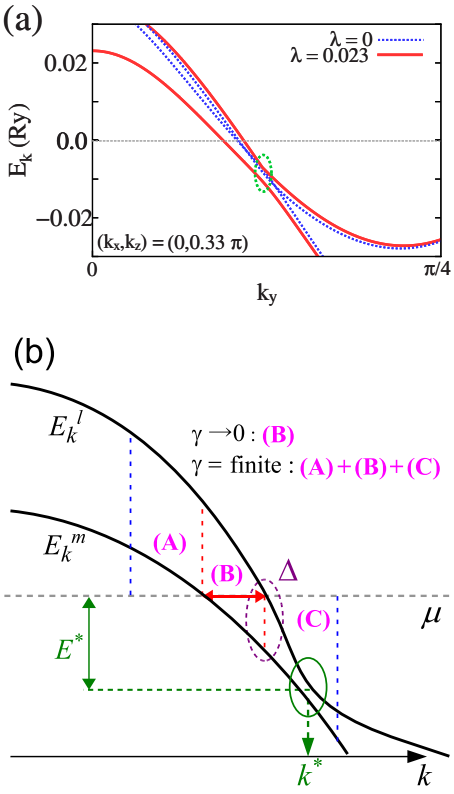

FIG. 10. (Color online) (a) Anticrossing bands in the NRL-TB model for Ta. We find an accidental degenerate point at $(k_x,k_y,k_z)=(0,0.12\pi,0.33\pi)$ in the present model with $\lambda=0$. The band splitting at $\boldsymbol{k}^*$ is $\sim$0.003. (b) Band structure around an accidental degenerate point slightly away from the Fermi level. The regions where $\boldsymbol{k}$ summation is performed for $\gamma\to 0$ and finite γ are represented by (A), (B), and (C). Δ represents the band splitting measured from the Fermi level and $\boldsymbol{k}^*$ represents the point of the minimum band splitting around the accidental degenerate point.

In Ta, there are several accidental degenerate points with $\lambda=0$ slightly away from the Fermi level. We show the anticrossing bands of NRL-TB model for Ta in Fig. 10(a). We find an accidental degenerate point at $(k_x,k_y,k_z)=(0,0.12\pi,0.33\pi)$ in the present model with $\lambda=0$. Note that this degeneracy splits with $\lambda\neq 0$, as recognized in Fig. 10(a).

In usual band structures, we have shown that the dominant contribution arises from the Fermi surface term σ_{xy}^{zI} and that the relation given by Eq. (44) holds well. On the other hand, in the exceptional case such as in Ta, the anomalous γ dependence of SHC can be explained by analyzing σ_{xy}^{zIIb} as follows: By dropping the current operators in Eq. (19) for simplicity, σ_{xy}^{zIIb} is given by

$$\sigma_{xy}^{zIIb}\propto\sum_{k,l>m}\frac{1}{(E_{\boldsymbol{k}}^l-E_{\boldsymbol{k}}^m)^2}\mathrm{Im}\left\{\ln\left(\frac{E_{\boldsymbol{k}}^l-i\gamma}{E_{\boldsymbol{k}}^m-i\gamma}\right)\right\}. \quad (46)$$

For $\gamma\ll|E_{\boldsymbol{k}}^l|$ $|E_{\boldsymbol{k}}^m|$, we can approximate as follows,

$$\mathrm{Im}\left\{\ln\left(\frac{E_{\boldsymbol{k}}^l-i\gamma}{E_{\boldsymbol{k}}^m-i\gamma}\right)\right\}\approx-\pi\theta(-E_{\boldsymbol{k}}^l)+\pi\theta(-E_{\boldsymbol{k}}^m)+\frac{\gamma(E_{\boldsymbol{k}}^l-E_{\boldsymbol{k}}^m)}{E_{\boldsymbol{k}}^lE_{\boldsymbol{k}}^m}. \quad (47)$$

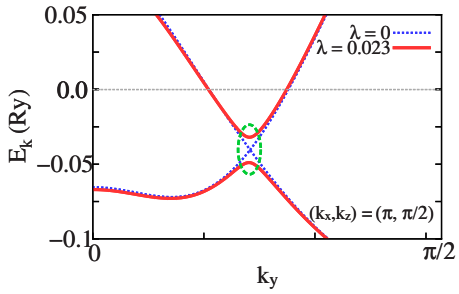

FIG. 11. (Color online) Anticrossing bands near the Fermi level with $\lambda=0$ and 0.023 in Ta: The k_y dependence of $E_{\boldsymbol{k}}^l$ for $(k_x,k_z)=(\pi,\pi/2)$ is shown. In the present model with $\lambda=0$, we find an accidental degenerate point at $(k_x,k_y,k_z)=(\pi,0.23\pi,\pi/2)$, which is different point from that shown in Fig. 10(b). The corresponding minimum band splitting induced by SOI is ~0.015.

By substituting the above equation into Eq. (46), we obtain the following relation for small γ:

$$\sigma_{xy}^{zIIb} \propto \sum_{k,l>m} \left[\frac{\theta(-E_{\boldsymbol{k}}^m) - \theta(-E_{\boldsymbol{k}}^l)}{(E_{\boldsymbol{k}}^l - E_{\boldsymbol{k}}^m)^2} + \gamma \frac{\theta(|E_{\boldsymbol{k}}^l| - \gamma)\theta(|E_{\boldsymbol{k}}^m| - \gamma)}{E_{\boldsymbol{k}}^l E_{\boldsymbol{k}}^m (E_{\boldsymbol{k}}^l - E_{\boldsymbol{k}}^m)} \right], \tag{48}$$

where the step function of the second term in the above equation is introduced to skip the $\boldsymbol{k}$ summation in the case of $\gamma \geqslant |E_{\boldsymbol{k}}^l|, |E_{\boldsymbol{k}}^m|$.

Figure 10(b) is a schematic band structure around the accidental degenerate point slightly away from the Fermi level. In this figure, Δ represents the band splitting measured from the Fermi level and E^* represents the eigenenergy measured from the Fermi level: $E^*=E_{\boldsymbol{k}*}^l \simeq E_{\boldsymbol{k}*}^m$.

The first term of Eq. (48) is finite only in region (B) where $E_{\boldsymbol{k}}^l>0$ and $E_{\boldsymbol{k}}^m<0$, and its sign is positive. The sign of the second term is negative in region (B), whereas it is positive in regions (A) and (C). When $\gamma \to 0$, σ_{xy}^{zIIb} is given only by the first term in Eq. (48) since the second term vanishes. When $E^* \sim \gamma$, a large contribution to σ_{xy}^{zIIb} comes from the second term in Eq. (48) from regime (C) in Fig. 10(b). Since the second term can be as large as the first term, σ_{xy}^{zIIb} takes the sizable peak at finite γ in the presence of almost degenerate anticrossing points near the Fermi level. The SHC reaches the maximum value at $\gamma \sim E^*$. As a result, the anomalous behavior of SHC in the NRL-TB model for Ta originates from the anticrossing points, as shown in Fig. 10(a). From this figure, we see that E_{k*}^l is ~0.01. This fact is consistent with the peak of SHC σ_{xy}^z at around $\gamma=0.02$ in Fig. 7(a).

In the present model with $\lambda=0$, there is another accidental degenerate point at $(k_x,k_y,k_z)=(\pi,0.23\pi,\pi/2)$. The band structure obtained for the NRL-TB model in Ta with $\lambda=0$ and $\lambda=0.023$ around this point is shown in Fig. 11. From this figure, when μ is lowered to $\Delta\mu=-0.04$, we see that the Fermi level begins to lie inside the gap. This fact causes a sharp peak of σ_{xy}^{zIIb} at $\Delta\mu=-0.04$ in Fig. 8(b).

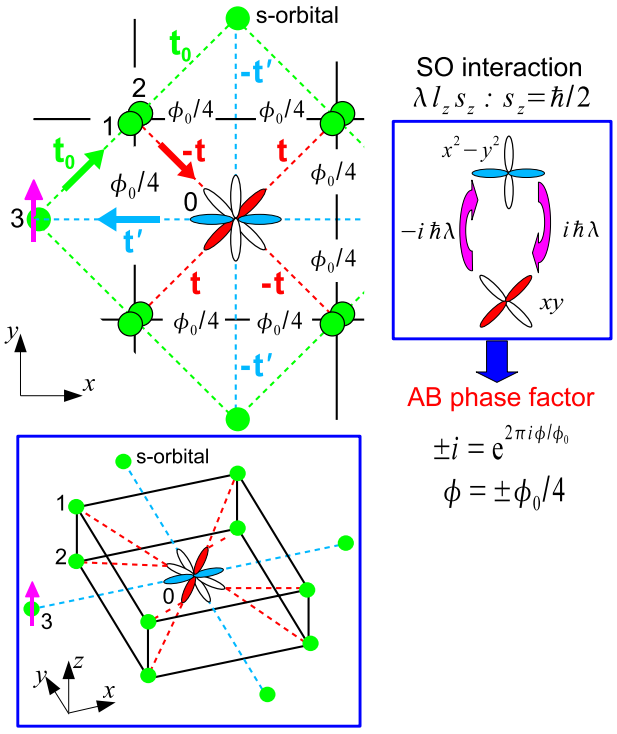

FIG. 12. (Color online) Effective AB phase in a double layer bcc model for a ↑-spin electron. This is the origin of the huge Hall conductivities in various transition metals.

Here, we have shown that the presence of almost degenerate anticrossing points in Ta gives rise to the anomalous γ dependence in the low resistive regime based on the NRL-TB model. In this exceptional situation, σ_{xy}^{zIIb} plays a significant role. Except for this special case, however, SHC is mainly given by the Fermi surface term σ_{xy}^{zI}. We may have to confirm this anomalous behavior in Ta by checking the accuracy of the NRL-TB model in detail.

V. DISCUSSIONS

A. Effective magnetic flux

In the previous section, we have discussed the SHC based on a multiorbital tight-binding model by using the Green function method. In this section, we give an intuitive reason why a huge SHC appears in the present multiorbital model based on the double layer bcc model in Fig. 12, which is a simplified version of the bcc structure model. Here, we consider only d_{xy}, $d_{x^2-y^2}$, and s orbitals considering the fact that d_{xy} and $d_{x^2-y^2}$ orbitals give the dominant contributions to the SHC in various transition metals, as explained in Sec. IV. In Fig. 12, $\pm t$ represents the hopping integrals between nearest neighbor d_{xy} and s orbitals, and $\pm t'$ is for the next nearest neighbor $d_{x^2-y^2}$ and s orbitals. Note that both hopping integrals change their signs by rotation by $\pi/2$. t_0 represents the hopping integral between s orbitals.

First, we explain that the electron can transfer from a $d_{x^2-y^2}$-orbital state to a d_{xy}-orbital state and vice versa by using SOI for ↑-spin electron $\hbar\lambda\hat{l}_z/2$, which plays a significant role in the large SHE and OHE in transition metals.[8]

The $|x^2-y^2\rangle$ state is transferred to the $|xy\rangle$ state by rotating the wave function around the z axis by $\pi/4$. Since $\hat{l}_z$ is a generator of the rotation operator about the z axis $\hat{R}_z(\theta)=e^{-i\theta\hat{l}_z}$, the relation between $\hat{l}_z$ and $\hat{R}_z(\theta)$ is given by

$$\mp\frac{i}{2}\hat{l}_z=\hat{R}_z\left(\pm\frac{\pi}{4}\right) \tag{49}$$

for the $l_z=\pm 2$ basis. Therefore,

$$\hat{l}_z|x^2-y^2\rangle=2i\hat{R}_z\left(\frac{\pi}{4}\right)|x^2-y^2\rangle=2i|xy\rangle, \tag{50}$$

$$\hat{l}_z|xy\rangle=-2i\hat{R}_z\left(\frac{\pi}{4}\right)|xy\rangle=-2i|x^2-y^2\rangle. \tag{51}$$

As a result, we obtain the off-diagonal matrix element of SOI for $\uparrow$-spin electron as follows:

$$\langle xy|\hbar\lambda\hat{l}_z/2|x^2-y^2\rangle=-\langle x^2-y^2|\hbar\lambda\hat{l}_z/2|xy\rangle=i\hbar\lambda. \tag{52}$$

Figure 12 shows the most important process (interorbital hopping process) for SHE in real space. By considering the signs of interorbital hopping integrals ($\pm t$ and $\pm t'$) and matrix elements of SOI in Eq. (52), we can verify that a clockwise (counterclockwise) movement of a $\uparrow$-spin electron along the path "$0\rightarrow 3\rightarrow 1$ or $2\rightarrow 0$," for example, causes the factor $+i$ $(-i)$. This factor can be interpreted as the Aharonov–Bohm phase factor $e^{2\pi i\phi/\phi_0}$ $[\phi_0=hc/|e|]$, where ϕ represents the effective magnetic flux $\phi=\oint\mathbf{A}d\mathbf{r}=\pm\phi_0/4$. Since the effective magnetic flux for $\downarrow$-spin electron is opposite in sign, electrons with different spins move in the opposite direction. Therefore, the effective magnetic flux gives rise to the SHC of order $O(\lambda)$. This mechanism will be realized in various multiorbital transition metals.[7,8]

B. Coherent-incoherent crossover of intrinsic Hall conductivities

In Sec. IV, we studied the γ dependence of the SHC in Ta and W numerically. Therein, we have verified that a typical crossover behavior of the intrinsic SHC at $\gamma\sim\Delta$ is realized in many transition metals unless almost degenerate anticrossing points exist slightly away from the Fermi level. This crossover behavior of σ_{xy} was shown in Refs. 15 and 22 Here, we analytically discuss the crossover behavior of intrinsic Hall conductivities by dividing into three regimes with respect to γ: $\gamma\ll\Delta$, $\Delta\ll\gamma\ll W$, and $W\ll\gamma$, where Δ and W represent the band splitting near the Fermi level and the bandwidth, respectively. The first regime corresponds to the low resistive regime, and the second to the high resistive regime. Here, we discuss the regime $W\ll\gamma$ only briefly since the Ioffe–Regel condition $\gamma\sim W$ is violated.

Now, we analyze Eqs. (16), (18), and (19) to obtain the γ dependence of the Fermi surface term σ_{xy}^{I} and the Fermi sea term σ_{xy}^{II}. The γ dependence of σ_{xy}^{I} is estimated by analyzing Eq. (16) for $\gamma\ll W$ by considering the following relationship:

TABLE III. γ dependence of the Fermi surface term σ_{xy}^{I}, Fermi sea terms σ_{xy}^{IIa} and σ_{xy}^{IIb} and the longitudinal conductivity σ_{xx}.

	$\gamma\ll\Delta$ (low ρ)	$\Delta\ll\gamma\ll W$ (high ρ)	$W\ll\gamma$
σ_{xy}^{I}	γ^0	γ^{-2}	γ^{-3}
σ_{xy}^{IIa}	γ^0	γ^0	γ^{-1}
σ_{xy}^{IIb}	γ^0	γ^0	γ^{-1}
σ_{xx}	γ^{-1}	γ^{-1}	γ^{-2}

$$\mathrm{Im}\left\{\frac{1}{(E^l-i\gamma)(E^m+i\gamma)}\right\}=\frac{\gamma(E_{\boldsymbol{k}}^l-E_{\boldsymbol{k}}^m)}{[(E_{\boldsymbol{k}}^l)^2+\gamma^2][(E_{\boldsymbol{k}}^m)^2+\gamma^2]} \tag{53a}$$

$$\approx\frac{\pi}{\gamma}\frac{\gamma(E_{\boldsymbol{k}}^m-E_{\boldsymbol{k}}^l)[\delta(E_{\boldsymbol{k}}^l)+\delta(E_{\boldsymbol{k}}^m)]}{(E_{\boldsymbol{k}}^m-E_{\boldsymbol{k}}^l)^2+\gamma^2}. \tag{53b}$$

After $\boldsymbol{k}$ summation, Eq. (53b) is proportional to γ^0 for $\gamma\ll\Delta$ and is proportional to γ^{-2} for $\Delta\ll\gamma\ll W$. On the other hand, in the regime $W\ll\gamma$, we can estimate Eq. (53a) as

$$\sum_{\boldsymbol{k}}\frac{\gamma(E_{\boldsymbol{k}}^l-E_{\boldsymbol{k}}^m)}{[(E_{\boldsymbol{k}}^l)^2+\gamma^2][(E_{\boldsymbol{k}}^m)^2+\gamma^2]}\sim\frac{\gamma}{\gamma^4}\sum_{\boldsymbol{k}}(E_{\boldsymbol{k}}^l-E_{\boldsymbol{k}}^m)\sim\gamma^{-3}. \tag{54}$$

In a similar way, the γ dependence of the Fermi sea terms σ_{xy}^{IIa} and σ_{xy}^{IIb} can be estimated from Eqs. (18) and (19), respectively. The longitudinal conductivity σ_{xx} is given by

$$\sigma_{xx}=\frac{1}{2\pi N}\sum_{\boldsymbol{k}}\mathrm{Tr}\left[\hat{J}_x^C\hat{G}^R\hat{J}_x^C\hat{G}^A-\frac{1}{2}\{\hat{J}_x^C\hat{G}^R\hat{J}_x^C\hat{G}^R+\langle R\leftrightarrow A\rangle\}\right]. \tag{55}$$

In Table III, the γ dependences of σ_{xy}^{I}, σ_{xy}^{IIa}, σ_{xy}^{IIb}, and σ_{xx} are shown. In the metallic systems, the relations $\sigma_{xy}\approx\sigma_{xy}^{I}$ (Fermi surface term) and $|\sigma_{xy}^{I}|\gg|\sigma_{xy}^{II}|$ hold well for a wide range of γ since the Fermi sea terms σ_{xy}^{IIa} and σ_{xy}^{IIb} almost cancel each other.[22] Therefore, we discuss the γ dependence of the Fermi surface term in detail. From Table III, the Fermi surface term σ_{xy}^{I} is independent of γ in the low resistive regime, whereas σ_{xy}^{I} decreases approximately proportional to γ^{-2} in the high resistive regime. On the other hand, the longitudinal conductivity σ_{xx} decreases approximately proportional to γ^{-1} in both low and high resistive regimes. Therefore, the coherent-incoherent crossover behavior of intrinsic Hall conductivities at $\gamma\sim\Delta$ are reproduced by considering the Fermi surface term σ_{xy}^{I} correctly, as reported in Refs. 15 and 22:

$$\sigma_{xy}\propto\sigma_{xx}^0 \quad \text{for } \gamma\ll\Delta, \tag{56}$$

$$\sigma_{xy}\propto\sigma_{xx}^2 \quad \text{for } \Delta\ll\gamma\ll W. \tag{57}$$

In the case of $W\ll\gamma$, the relation $\sigma_{xy}\propto\sigma_{xx}^{1.5}(\propto\gamma^{-3})$ holds. However, this relation is not reliable since the Ioffe–Regel condition $(W/\gamma\sim E_F\tau\leqslant 1)$ is violated in this regime.[50]

Finally, we comment on the σ_{xy}^{IIb} term, which is called the Berry curvature term. In electron gas models, the relation $\sigma_{xy}=\sigma_{xy}^{IIb}$ holds for $\gamma=+0$ since $\sigma_{xy}^{I}+\sigma_{xy}^{IIa}=0$.[18,19] However,

$\sigma_{xy} \neq \sigma_{xy}^{IIb}$ for finite γ, and the crossover behavior cannot be explained by analyzing σ_{xy}^{IIb}, which is shown in Table III. In conclusion, the relationship $\sigma_{xy} \approx \sigma_{xy}^{I}$ and $|\sigma_{xy}^{I}| \gg |\sigma_{xy}^{II}|$ hold well in the real metallic systems, and the correct crossover behavior given by Eqs. (56) and (57) are reproduced by the Fermi surface term σ_{xy}^{I}.

Now, we comment on the Ioffe–Regel limit in transition metals: The Ioffe–Regel limit $l/a \sim k_F l \sim 1$ is approximately estimated as $E_F/\gamma \sim 1$, where l, a, k_F, E_F, and γ represents an elastic mean free path, a lattice constant, a Fermi wave number, a Fermi energy, and a quasiparticle damping rate, respectively. From the band structure for Ta and Pt in the present model, we verified that E_F is ~ 1 in Ta and ~ 0.5 in Pt. Therefore, the Ioffe–Regel limit lies at around $\gamma \sim 1$ in Ta and at $\gamma \sim 0.5$ in Pt, respectively. Since the localization effect of the electron is not taken into account, the present calculation will be inadequate for $E_F/\gamma \gg 1$.

VI. SUMMARY

In this paper, we studied the intrinsic SHE and OHE in various $4d$ transition metals (Nb, Mo, Tc, Ru, Rh, Pd, and Ag) and $5d$ transition metals (Ta, W, Re, Os, Ir, Pt, and Au) based on a multiorbital tight-binding model. We derived the general expressions for the intrinsic SHC and OHC in the presence of overlap integrals given by Eq. (5). We found that the huge SHCs in Pt ($5d^9 6s^1$) and Pd ($4d^{10} 5s^0$) are positive, whereas the SHCs in Ta ($5d^3 6s^2$) and W ($5d^4 6s^2$) take large negative values. We also found that the SHC changes smoothly with the electron number $n=n_s+n_d$, regardless of the changes of the crystal structure. Among the $4d$ and $5d$ transition metals, the magnitude of SHC in Pt shows the largest value in the low resistive regime. However, the magnitude of SHC in Ta and W exceeds that in Pt in the high resistive regime. Therefore, large negative values of SHCs in Ta and W will be observed even in the high resistive samples. In this paper, we also calculated the SHC for $n=7$ and 8 (hcp structure).

We also showed that the CVC due to the local impurity potential can be safely neglected in calculating the SHC and OHC in the present model. The obtained SHCs in various transition metals are sensitive to the changes of the chemical potential μ, which reflect the multiband structure around the Fermi level μ. This suggests that the intrinsic SHC can be controlled by composing alloys. As for the γ dependences of SHC and OHC, we obtained the coherent-incoherent crossover behaviors in many transition metals by calculating both Fermi surface and Fermi sea terms on the same footing: σ_{xy}^{z} is independent of γ in the low resistive regime where $\gamma \ll \Delta$, whereas σ_{xy}^{z} decreases approximately proportional to ρ^{-2} in the high resistive regime. The physical meaning of the crossover behavior can be explained as follows: In the low resistive regime, SHC is proportional to the lifetime of the interband excitation $\hbar/\Delta$ since it is caused by the interband particle-hole excitation induced by the electric field.[5–7,10,15,22] However, in the high resistive regime, SHC decreases with γ since the quasiparticle lifetime $\hbar/\gamma$ becomes shorter than $\hbar/\Delta$.[15,22]

Here, we comment on the effect of Coulomb interaction on the SHC and OHC. In the microscopic Fermi liquid theory, the Coulomb interaction is renormalized to the self-energy correction and the CVC. The renormalization factor due to the self-energy, $z=(1-\frac{\partial \Sigma(\omega)}{\partial \omega}|_{\omega=0})^{-1}$ exactly cancels in the final formulas of the SHC and OHC, i.e., Eqs. (16), (18), and (19). As shown in Ref. 15 the CVC due to the Coulomb interaction does not cause the skew scattering. Therefore, γ dependences of intrinsic SHC and OHC are unchanged by the CVC due to Coulomb interactions. However, it is well known that the CVC causes various anomalous transport phenomena in the vicinity of the magnetic quantum critical points (QCPs).[51–55] In the same way, a prominent CVC near the magnetic QCP may cause a different temperature dependence of the SHC and OHC. This is an important future problem.

Owing to the present study of SHE and OHE in various transition metals, it has been revealed that the huge SHE and OHE are ubiquitous in multiorbital d-electron systems. In Sec. V A, we discussed that the origin of these huge SHE is the "effective AB phase" induced by the atomic SOI with the aid of interorbital hopping integrals.[7,8] The present study strongly suggests that "giant SHE and OHE" will be seen ubiquitously in multiorbital f-electron systems with atomic orbital degrees of freedom. These facts will enable us to construct efficient spintronics or orbitronics devices made of transition metals. Furthermore, in f-electron systems, a larger SHE may appear as compared to that in d-electron systems since the angular momentum of the atomic orbital is larger and the band splitting near the Fermi surface is smaller.

In the presence of anticrossing bands, a huge SHC can be realized when the Fermi level lies inside the gap induced by SOI.[30,31] In this case, $\sigma_{xy}^{I}=0$ and σ_{xy}^{II} takes a large (and almost quantized) value. In the present study, however, we could not find any elemental metals in which the Dirac-cone-type band structure has a dominant contribution to SHE in the low resistive regime. The large SHCs in transition metals are mainly given by the Fermi surface term, σ_{xy}^{I}. Therefore, the existence of a Dirac point is not a necessary condition for a large SHE: As shown in Fig. 9, the band structure where the band splitting near the Fermi level is small is significant for a large SHE. However, only in the case of Ta, almost degenerate anticrossing points that exist slightly away from the Fermi level give rise to an anomalous γ dependence in the low resistive regime. The anomalous γ dependence of SHC in Ta may be realized.

Finally, we discuss the quantitative accuracy of the obtained numerical results, which depends on the accuracy of the band structure of the model near the Fermi level. SHC and OHC depend on the multiband structure near the Fermi level with a small interband splitting Δ, and they are proportional to Δ^{-1} according to Eq. (16). According to Ref. 42, the possible error in the NRL-TB model is about 0.002–0.004 Ry, which is much smaller than Δ ($\Delta \sim 0.035$ Ry in Pt), which gives the minimum energy scale in the intrinsic Hall effect. Therefore, it is expected that the NRL-TB model is accurate enough to qualitatively derive reliable results of SHC and OHC. Thus, the overall n dependence of the SHC in Fig. 5 will be reliable.

ACKNOWLEDGMENTS

We are grateful to D. A. Papaconstantopoulos and I. Mazin for useful comments and discussions on the NRL-TB model. We also thank H. Aoki, H. Fukuyama, M. Ogata, and E. Saitoh for fruitful discussions. This study has been supported by Grants-in-Aid for Scientific Research from the Ministry of Education, Culture, Sports, Science and Technology of Japan. Numerical calculations were performed at the facilities of the Supercomputer Center, ISSP, University of Tokyo.

APPENDIX A: DERIVATION OF EQUATION (38)

Here, we derive Eq. (38). $n(\boldsymbol{q})$ is given by a Fourier transform of the electron number density $n(\boldsymbol{r})$ as follows:

$$n(\boldsymbol{q}) = \int d\boldsymbol{r} n(\boldsymbol{r}) e^{-i\boldsymbol{q}\boldsymbol{r}} = \int d\boldsymbol{r} \psi^{\dagger}(\boldsymbol{r}) \psi(\boldsymbol{r}) e^{-i\boldsymbol{q}\boldsymbol{r}}$$
$$= \sum_{\boldsymbol{k},\boldsymbol{k}'} \sum_{\alpha,\beta} \left[\int d\boldsymbol{r} \phi^{*}_{\boldsymbol{k}\alpha}(\boldsymbol{r}) \phi_{\boldsymbol{k}'\beta}(\boldsymbol{r}) e^{-i\boldsymbol{q}\boldsymbol{r}} \right] c^{\dagger}_{\boldsymbol{k}\alpha} c_{\boldsymbol{k}'\beta}, \quad \text{(A1)}$$

where $\psi(\boldsymbol{r})$ represents the electron field operator; this operator can be expanded with the atomic wave function $\phi_{kl}(\boldsymbol{r})$ as follows:

$$\psi(\boldsymbol{r}) = \sum_{\boldsymbol{k},\alpha} \phi_{\boldsymbol{k}\alpha}(\boldsymbol{r}) c_{\boldsymbol{k}\alpha}. \quad \text{(A2)}$$

We used this relation to transfer from the second row to the third row in Eq. (A1).

From Bloch's theorem, the atomic wave function can be rewritten as

$$\phi_{\boldsymbol{k}\alpha}(\boldsymbol{r}) = \frac{1}{\sqrt{N}} u_{\boldsymbol{k}\alpha}(\boldsymbol{r}) e^{i\boldsymbol{k}\cdot\boldsymbol{r}}, \quad \text{(A3)}$$

where

$$u_{\boldsymbol{k}\alpha}(\boldsymbol{r}) = \sum_{i} e^{i\boldsymbol{k}(\boldsymbol{R}_i - \boldsymbol{r})} \phi_{\alpha}(\boldsymbol{r} - \boldsymbol{R}_i). \quad \text{(A4)}$$

Then, it is straightforward to show that the equation in square bracket in Eq. (A1) is rewritten as

$$\delta(\boldsymbol{k} + \boldsymbol{q} - \boldsymbol{k}') \int_{unit} d\boldsymbol{r} u^{*}_{\boldsymbol{k}\alpha}(\boldsymbol{r}) u_{\boldsymbol{k}'\beta}(\boldsymbol{r}). \quad \text{(A5)}$$

Therefore, Eq. (A1) is rewritten as

$$\sum_{\boldsymbol{k},\alpha,\beta} \left[\int_{unit} d\boldsymbol{r} u^{*}_{\boldsymbol{k}\alpha}(\boldsymbol{r}) u_{\boldsymbol{k}+\boldsymbol{q},\beta}(\boldsymbol{r}) \right] c^{\dagger}_{\boldsymbol{k}\alpha} c_{\boldsymbol{k}+\boldsymbol{q},\beta}. \quad \text{(A6)}$$

Here, we expand $[\cdot]$ in Eq. (A6) in powers of $q/2 (q = |\boldsymbol{q}|)$ as follows:

$$\int_{unit} d\boldsymbol{r} u^{*}_{\boldsymbol{k}+(\boldsymbol{q}/2)-\boldsymbol{q}+2,\alpha}(\boldsymbol{r}) u_{\boldsymbol{k}+(\boldsymbol{q}/2)+(\boldsymbol{q}/2),\beta}(\boldsymbol{r})$$
$$= \int_{unit} d\boldsymbol{r} u^{*}_{\tilde{\boldsymbol{k}}\alpha} u_{\tilde{\boldsymbol{k}}\beta} + \frac{q}{2} A_{\alpha\beta} + O\left(\frac{\boldsymbol{q}}{2}\right), \quad \text{(A7)}$$

where $\tilde{\boldsymbol{k}}$ is given by $\tilde{\boldsymbol{k}} = \boldsymbol{k} + (\boldsymbol{q}/2)$, and $\frac{q}{2} A_{\alpha\beta}$ is given by

$$\int_{unit} d\boldsymbol{r} \sum_{i,j} \left[\frac{\boldsymbol{q}}{2} (\boldsymbol{R}_i - \boldsymbol{r}) e^{-i\tilde{\boldsymbol{k}}(\boldsymbol{R}_i - \boldsymbol{r})} \phi^{*}_{\alpha}(\boldsymbol{r} - \boldsymbol{R}_i) e^{i\tilde{\boldsymbol{k}}(\boldsymbol{R}_j - \boldsymbol{r})} \phi_{\beta}(\boldsymbol{r} - \boldsymbol{R}_j) \right.$$
$$\left. + \frac{\boldsymbol{q}}{2} (\boldsymbol{R}_j - \boldsymbol{r}) e^{-i\tilde{\boldsymbol{k}}(\boldsymbol{R}_i - \boldsymbol{r})} \phi^{*}_{\alpha}(\boldsymbol{r} - \boldsymbol{R}_i) e^{i\tilde{\boldsymbol{k}}(\boldsymbol{R}_j - \boldsymbol{r})} \phi_{\beta}(\boldsymbol{r} - \boldsymbol{R}_j) \right]. \quad \text{(A8)}$$

First, the first term on the right hand side in Eq. (A7) can be calculated as follows:

$$\int_{unit} d\boldsymbol{r} \sum_{i,j} e^{-i\tilde{\boldsymbol{k}}(\boldsymbol{R}_i - \boldsymbol{r})} \phi^{*}_{\alpha}(\boldsymbol{r} - \boldsymbol{R}_i) e^{i\tilde{\boldsymbol{k}}(\boldsymbol{R}_j - \boldsymbol{r})} \phi_{\beta}(\boldsymbol{r} - \boldsymbol{R}_j) = O^{-1}_{\alpha\beta}(\tilde{\boldsymbol{k}}). \quad \text{(A9)}$$

Next, we show that $\frac{q}{2} A_{\alpha\beta}$ given by Eq. (A8) vanishes by rewriting Eq. (A8) as follows:

$$\sum_{\tilde{\boldsymbol{k}}'} \delta_{\tilde{\boldsymbol{k}}\tilde{\boldsymbol{k}}'} \frac{\boldsymbol{q}}{2} \cdot \left(\frac{\partial}{\partial \tilde{\boldsymbol{k}}} - \frac{\partial}{\partial \tilde{\boldsymbol{k}}'} \right) \left[\int_{unit} d\boldsymbol{r} \sum_{i,j} e^{-i\tilde{\boldsymbol{k}}(\boldsymbol{R}_i - \boldsymbol{r})} \right.$$
$$\left. \times \phi^{\dagger}_{\alpha}(\boldsymbol{r} - \boldsymbol{R}_i) e^{i\tilde{\boldsymbol{k}}'(\boldsymbol{R}_j - \boldsymbol{r})} \phi_{\beta}(\boldsymbol{r} - \boldsymbol{R}_j) \right]$$
$$= \frac{\boldsymbol{q}}{2N} \cdot \left(\frac{\partial}{\partial \tilde{\boldsymbol{k}}} O^{-1}_{\alpha\beta} - \frac{\partial}{\partial \tilde{\boldsymbol{k}}} O^{-1}_{\alpha\beta} \right) = 0. \quad \text{(A10)}$$

Therefore, the final result for $n(\boldsymbol{q})$ is given by

$$n(\boldsymbol{q}) = \sum_{\boldsymbol{k},\alpha,\beta} O^{-1}_{\alpha\beta}(\boldsymbol{k}) c^{\dagger}_{\boldsymbol{k}-(\boldsymbol{q}/2),\alpha} c_{\boldsymbol{k}+(\boldsymbol{q}/2),\beta}, \quad \text{(A11)}$$

which is exact up to $O(q)$.

APPENDIX B: DEFINITIONS OF SPIN AND ORBITAL CURRENT OPERATORS

In the present study, we assume that the spin and orbital current operators are given by Eqs. (11) and (12) according to literature.[24,47] Here, we show the validity for these definitions in a microscopic way. Since the spin and orbital operators are not conserved in the present model with SOI, we cannot define spin and orbital current operators from the continuity equations. However, it is possible to make a natural definition for each current operator, as follows.

First, we consider the spin current operator. Since the SOI in the present model is local, we can virtually apply a magnetic field (vector potential) to ↑-spin and ↓-spin electrons separately. Here, we denote the vector potential for ↑ spin and ↓ spin as $\boldsymbol{A}_{\uparrow}$ and $\boldsymbol{A}_{\downarrow}$, respectively. By considering a transformation $\boldsymbol{k}_{\sigma} \rightarrow \boldsymbol{k}_{\sigma} - e\boldsymbol{A}_{\sigma}$, where σ is a spin index, the x component of current operators for ↑-spin and ↓-spin electrons are given by

$$J_{\uparrow x} = \frac{\partial \hat{H}}{\partial A_{\uparrow x}} = -e \begin{pmatrix} v_x & 0 \\ 0 & 0 \end{pmatrix}, \quad \text{(B1)}$$

$$J_{\downarrow x} = \frac{\partial \hat{H}}{\partial A_{\downarrow x}} = -e \begin{pmatrix} 0 & 0 \\ 0 & v_x \end{pmatrix}. \quad \text{(B2)}$$

Therefore, the natural definition of a spin current operator in the present model is given by

$$J_x^S = \frac{1}{(-e)}(J_{\uparrow x} - J_{\downarrow x}). \tag{B3}$$

This expression is equivalent to Eq. (11). We note that the above discussion cannot be applied to systems in the presence of nonlocal SOI, such as a Rashba type SOI.

Next, we consider the orbital current operator. The charge current operator $J_x^C = J_{\uparrow x} + J_{\downarrow x}$ is expressed in the real space representation as

$$\boldsymbol{J}^C = \sum_{im,jm'} \boldsymbol{J}^C_{im,jm'}, \tag{B4}$$

$$\boldsymbol{J}^C_{im,jm'} = -e(\boldsymbol{r}_i - \boldsymbol{r}_j) \cdot t_{im,jm'}(c^\dagger_{im} c_{jm'} - c^\dagger_{jm'} c_{im}), \tag{B5}$$

where i is the position of ith lattice point, m represents the eigenvalue of $\hat{l}_z$, and $t_{im,jm'}$ represents the hopping integral between $|m\rangle$ state at ith site and $|m'\rangle$ state at jth site, respectively. Then, the natural definition of the orbital current operator will be given by

$$(\boldsymbol{J}^O)_{im,jm'} = \frac{1}{2(-e)}(m + m')(\boldsymbol{J}^C)_{im,jm'}, \tag{B6}$$

in the basis of $l_z = 2, 1, \ldots, -2$. By performing Fourier transforms of Eq. (B6), we obtain the following expression for the orbital current operator in the present model:

$$(\boldsymbol{J}^O(\boldsymbol{k}))_{mm'} = \frac{1}{2(-e)}(m + m')(\boldsymbol{J}^C(\boldsymbol{k}))_{m,m'}. \tag{B7}$$

In a general basis, the above equation can be rewritten as

$$\boldsymbol{J}^O = \{\boldsymbol{J}^C, l_z\}/2(-e). \tag{B8}$$

This expression is equivalent to Eq. (12). In summary, we have introduced a natural definition of the spin and orbital current operators, and we have shown that they are equivalent to Eqs. (11) and (12), respectively.

In the same manner, if we define the spin current operator (in the presence of the intersite SOI) as $(\boldsymbol{J}^S)_{im\sigma,jm'\sigma'} = \frac{1}{2(-e)}(\sigma + \sigma')(\boldsymbol{J}^C)_{im\sigma,jm'\sigma'}$, we can derive the spin current $\boldsymbol{J}^S = \{\boldsymbol{J}^C, s_z\}/2(-e)$ immediately. This is another microscopic derivation of the spin current operator in Eq. (11).

[1] E. Saitoh, M. Ueda, H. Miyajima, and G. Tatara, Appl. Phys. Lett. **88**, 182509 (2006).
[2] S. O. Valenzuela and M. Tinkham, Nature (London) **442**, 176 (2006).
[3] N. P. Stern, S. Ghosh, G. Xiang, M. Zhu, N. Samarth, and D. D. Awschalom, Phys. Rev. Lett. **97**, 126603 (2006).
[4] T. Kimura, Y. Otani, T. Sato, S. Takahashi, and S. Maekawa, Phys. Rev. Lett. **98**, 156601 (2007).
[5] S. Murakami, N. Nagaosa, and S. C. Zhang, Phys. Rev. B **69**, 235206 (2004).
[6] J. Sinova, D. Culcer, Q. Niu, N. A. Sinitsyn, T. Jungwirth, and A. H. MacDonald, Phys. Rev. Lett. **92**, 126603 (2004).
[7] H. Kontani, T. Tanaka, D. S. Hirashima, K. Yamada, and J. Inoue, Phys. Rev. Lett. **100**, 096601 (2008).
[8] H. Kontani, M. Naito, D. S. Hirashima, K. Yamada, and J. Inoue, J. Phys. Soc. Jpn. **76**, 10 (2007).
[9] G. Y. Guo, S. Murakami, T.-W. Chen, and N. Nagaosa, Phys. Rev. Lett. **100**, 096401 (2008).
[10] R. Karplus and J. M. Luttinger, Phys. Rev. **95**, 1154 (1954).
[11] M. I. Dyakonov and V. I. Perel, Sov. Phys. JETP **13**, 467 (1971); J. E. Hirsch Phys. Rev. Lett. **83**, 1834 (1999).
[12] J. M. Luttinger, Phys. Rev. **112**, 739 (1958).
[13] H. Fukuyama, Ph.D. thesis, University of Tokyo, 1970.
[14] N. A. Sinitsyn, A. H. MacDonald, T. Jungwirth, V. K. Dugaev, and J. Sinova, Phys. Rev. B **75**, 045315 (2007).
[15] H. Kontani and K. Yamada, J. Phys. Soc. Jpn. **63**, 2627 (1994).
[16] H. Kontani and K. Yamada, J. Phys. Soc. Jpn. **66**, 2252 (1997).
[17] M. Miyazawa, H. Kontani, and K. Yamada, J. Phys. Soc. Jpn. **68**, 1625 (1999).
[18] G. Sundaram and Q. Niu, Phys. Rev. B **59**, 14915 (1999).
[19] M. Onoda and N. Nagaosa, J. Phys. Soc. Jpn. **71**, 19 (2002).
[20] Y. Yao, L. Kleinman, A. H. MacDonald, J. Sinova, T. Jungwirth, D. S. Wang, E. Wang, and Q. Niu, Phys. Rev. Lett. **92**, 037204 (2004).
[21] Z. Fang, N. Nagaosa, K. Takahashi, A. Asamitsu, R. Mathieu, T. Ogasawara, H. Yamada, M. Kawasaki, Y. Tokura, and K. Terakura, Science **302**, 92 (2003).
[22] H. Kontani, T. Tanaka, and K. Yamada, Phys. Rev. B **75**, 184416 (2007).
[23] J. I. Inoue, T. Kato, Y. Ishikawa, H. Itoh, G. E. W. Bauer, and L. W. Molenkamp, Phys. Rev. Lett. **97**, 046604 (2006).
[24] J. I. Inoue, G. E. W. Bauer, and L. W. Molenkamp, Phys. Rev. B **70**, 041303 (2004).
[25] R. Raimondi and P. Schwab, Phys. Rev. B **71**, 033311 (2005).
[26] E. I. Rashba, Phys. Rev. B **70**, 201309(R) (2004).
[27] J. Smit, Physica (Amsterdam) **21**, 877 (1955).
[28] S. Murakami, Phys. Rev. B **69**, 241202(R) (2004).
[29] B. A. Bernevig and S.-C. Zhang, Phys. Rev. Lett. **95**, 016801 (2005).
[30] S. Murakami, N. Nagaosa, and S.-C. Zhang, Phys. Rev. Lett. **93**, 156804 (2004).
[31] C. L. Kane and E. J. Mele, Phys. Rev. Lett. **95**, 146802 (2005).
[32] M. J. Mehl and D. A. Papaconstantopoulos, Phys. Rev. B **54**, 4519 (1996).
[33] D. A. Papaconstantopoulos and M. J. Mehl, J. Phys.: Condens. Matter **15**, R413 (2003).
[34] T. Tanaka, H. Kontani, M. Naito, T. Naito, D. S. Hirashima, K. Yamada, and J. Inoue (unpublished).
[35] J. Smit, Physica (Amsterdam) **24**, 39 (1958).
[36] L. Berger, Phys. Rev. B **2**, 4559 (1970).
[37] M. I. D'yakonov and V. I. Perel, Zh. Eksp. Teor. Fiz. Pis'ma Red. **13**, 657 (1971).
[38] J. E. Hirsh, Phys. Rev. Lett. **83**, 1834 (1999).
[39] S. Zhang, Phys. Rev. Lett. **85**, 393 (2000).
[40] H.-A. Engel, E. I. Rashba, and B. I. Halperin, *Handbook of Magnetism and Advanced Magnetic Materials* (Wiley, New York,

2007) Vol. 5.
[41] J. C. Slater and G. F. Koster, Phys. Rev. **94**, 1498 (1954).
[42] D. A. Papaconstantopoulos and I. Mazin (private communication).
[43] J. Friedel P. Lenglart, and G. Leman, J. Phys. Chem. Solids **25**, 781 (1964).
[44] F. Herman and S. Skillman, *Atomic Structure Calculations* (Prentice-Hall, Englewood Cliffs, NJ, 1963).
[45] L. F. Mattheiss and R. E. Watson, Phys. Rev. Lett. **13**, 526 (1964).
[46] S. Bei der Kellen and A. J. Freemann, Phys. Rev. B **54**, 11187 (1996).
[47] G. Y. Guo, Y. Yao, and Q. Niu, Phys. Rev. Lett. **94**, 226601 (2005).
[48] P. Streda, J. Phys. C **15**, L717 (1982).
[49] M. Naito and D. S. Hirashima, J. Phys. Soc. Jpn. **76**, 044703 (2007).
[50] S. Onoda, N. Sugimoto, and N. Nagaosa, Phys. Rev. Lett. **97**, 126602 (2006). They seem to have derived the relation $\sigma_{xy} \propto \sigma_{xx}^{1.6}$ from the regime $E_F\tau \lesssim 1$, which may be outside the scope of the T-matrix approximation.
[51] H. Kontani, K. Kanki, and K. Ueda, Phys. Rev. B **59**, 14723 (1999).
[52] H. Kontani, J. Phys. Soc. Jpn. **70**, 1873 (2001).
[53] H. Kontani, J. Phys. Soc. Jpn. **70**, 2840 (2001).
[54] H. Kontani, Phys. Rev. Lett. **89**, 237003 (2002).
[55] H. Kontani, Rep. Prog. Phys. **71**, 026501 (2008); H. Kontani and K. Yamada, J. Phys. Soc. Jpn. **74**, 155 (2005).